Nonlinear stability and patterns in granular plane Couette flow: Hopf and pitchfork bifurcations, and evidence for resonance

PRIYANKA SHUKLA AND MEHEBOOB ALAM†

Engineering Mechanics Unit, Jawaharlal Nehru Centre for Advanced Scientific Research
Jakkur PO, Bengaluru 560064, India

The first evidence of a variety of nonlinear equilibrium states of travelling and stationary waves is provided in a two-dimensional granular plane Couette flow via nonlinear stability analysis. The relevant order-parameter equation, the Landau equation, has been derived for the most unstable two-dimensional perturbation of finite size. Along with the linear eigenvalue problem, the mean-flow distortion, the second harmonic, the distortion to the fundamental mode and the first Landau coefficient are calculated using a spectral-based numerical method. Two types of bifurcations, Hopf and pitchfork, that result from travelling and stationary instabilities, respectively, are analysed using the first Landau coefficient. The present bifurcation theory shows that the flow is subcritically unstable to stationary finite-amplitude perturbations of long wavelengths ($k_x \sim 0$, where k_x is the streamwise wavenumber) in the dilute limit that evolve from subcritical shear-banding modes ($k_x = 0$), but at large enough Couette gaps there are stationary instabilities with $k_x = O(1)$ that lead to supercritical pitchfork bifurcations. At moderate-to-large densities, in addition to supercritical shear-banding modes, there are long-wave travelling instabilities that lead to Hopf bifurcations. It is shown that both supercritical and subcritical nonlinear states exist at moderate-to-large densities that originate from the dominant stationary and travelling instabilities for which $k_x = O(1)$. Nonlinear patterns of density, velocity and granular temperature for all types of instabilities are contrasted with their linear eigenfunctions. While the supercritical solutions appear to be modulated forms of the fundamental mode, the structural features of unstable subcritical solutions are found to be significantly different from their linear counterparts. It is shown that the granular plane Couette flow is prone to nonlinear resonances in both stable and unstable regimes, the signature of which is implicated as a discontinuity in the first Landau coefficient. Our analysis identified two types of modal resonances that appear at the quadratic order in perturbation amplitude: (i) a 'mean-flow resonance' which occurs due to the interaction between a streamwise-independent shear-banding mode ($k_x = 0$) and a linear/fundamental mode $k_x \neq 0$, and (ii) an exact '1 : 2 resonance' that results from the interaction between two waves with their wavenumber ratio being 1 : 2.

Key words: granular media, nonlinear dynamical systems, nonlinear instability

† Email address for correspondence: meheboob@jncasr.ac.in

1. Introduction

1.1. *Pattern formation and order-parameter models for granular fluids*

Pattern-forming systems belong to a class of problems in which an external control parameter governs the system behaviour beyond the critical point. As the control parameter is increased above its critical value, the homogeneous state loses stability, giving rise to a new patterned state. A collection of particles, when subjected to strong external forcing, show a variety of dynamical patterns. For example, when a thin layer of granular materials is subjected to vertical harmonic oscillation, a range of standing wave patterns (squares, stripes, hexagon and interfaces), similar to Faraday waves, can be observed (Umbanhowar, Melo & Swinney 1996), depending on the shaking strength and its frequency. Moreover, a localized structure, 'oscillon', which is reminiscent of solitary waves in water (Umbanhowar *et al.* 1996), can appear via a hysteretic transition under certain external forcing conditions on the frequency and acceleration. In many experiments in the rapid flow regime, a variety of patterns such as longitudinal vortices (Forterre & Pouliquen 2002), Kelvin–Helmholtz instability (Goldfarb, Glasser & Shinbrot 2002) and convection from granular Leidenfrost state (Eshuis *et al.* 2010) have been observed; the onset of such patterns has been theoretically explained from linear stability analyses of pertinent hydrodynamic equations (Alam & Nott 1998; Forterre & Pouliquen 2002; Eshuis *et al.* 2010).

Tsimring & Aranson (1997) proposed a phenomenological order-parameter model, the Ginzburg–Landau equation coupled with an effective mass conservation equation, to theoretically study the patterns in a vibrated granular bed:

$$\frac{\partial \psi}{\partial t} = \gamma \tilde{\psi} - (1 - i\omega)\psi + (1 + ib)\nabla^2 \psi - |\psi|^2 \psi - \varrho\psi, \tag{1.1}$$

$$\frac{\partial \varrho}{\partial t} = \alpha \nabla \cdot \left(\varrho \nabla |\psi|^2\right) + \beta \nabla^2 \varrho. \tag{1.2}$$

Equation (1.1) is an evolution equation for a complex quantity $\psi(\boldsymbol{x}, t)$, called the *order-parameter* or the *amplitude* function; (1.2) represents an effective equation for the conservation of mass (average mass of granular material per unit area), with $\varrho(\boldsymbol{x}, t)$ being the mass density of granular materials. The last term in (1.1), $\varrho\psi$, represents a coupling between the order parameter and the local bulk density of material; the cubic nonlinear term $|\psi|^2\psi$ accounts for the nonlinear saturation of oscillations due to dissipation; the term involving the Laplacian accounts for any diffusive mechanism, providing a length scale for patterns.

The above order-parameter model is phenomenological in the sense that it has not been derived from the governing equations of granular fluids, and the coefficients in (1.1)–(1.2) have to be determined from experiments or simulations on a case-by-case basis. Note that the above model is strictly valid for flows in which the mean velocity is zero, such as in a vertically shaken bed under harmonic excitation, for which the momentum equation is identically satisfied. Information about the rheology of the flow needs to be supplemented, in addition to (1.1)–(1.2), via momentum balance equations (Aranson & Tsimring 2006). At any rate, the above order-parameter model has been able to interpret the experimental (and simulation) data in a variety of granular flows (see Aranson & Tsimring 2006 for a review; see Orpe & Khakhar 2007 for an application of this model to predict the rheology of surface flows in a rotating drum), thus lending support to derive such order-parameter equations from first principles.

Order-parameter equations such as the Ginzburg–Landau equation or the Swift–Hohenberg equation (Eckhaus 1965; Newell & Whitehead 1969; Stewartson & Stuart 1971; Stuart 1971; Busse 1978; Manneville 1990; Cross & Hohenberg 1993; Schmid & Henningson 2001; Mozorov & van Saarloos 2007) are widely used to study pattern-forming systems in many fields (such as superconductivity, superfluidity, vacancy diffusion, defect turbulence, convection, surface waves, and absolute and convective instabilities). For example, the Ginzburg–Landau equation (1.1), without the coupling term $\varrho\psi$, gives a model for the parametric instability in an oscillating liquid layer; in particular, the term $\gamma\tilde{\psi}$ ('tilde' denoting a complex conjugate quantity) accounts for the parametric driving that excites standing waves. As seen in (1.1), the order parameter $\psi(\boldsymbol{x}, t)$ is a function of space and time, and hence is suitable for describing *aperiodic* patterns having slow modulations in space and time.

For patterns having *spatial periodicity*, the Ginzburg–Landau equation reduces to the well-known Landau equation, which is an ordinary differential equation for a temporally varying order parameter $\psi(t) \equiv \psi(\boldsymbol{x}, t)$:

$$\frac{\mathrm{d}\psi}{\mathrm{d}t} = c^{(0)}\psi + c^{(2)}\psi|\psi|^2 + \cdots, \tag{1.3}$$

where the coefficients $c^{(0)} = a^{(0)} + \mathrm{i}b^{(0)}$ and $c^{(2)} = a^{(2)} + \mathrm{i}b^{(2)}$ are the linear eigenvalue and the first Landau coefficient (which represents the leading nonlinear correction to the linear mode), respectively. Developing an order-parameter theory via (1.3) to describe patterns in a granular plane Couette flow is the focus of the present paper.

1.2. *Patterns in a granular plane Couette flow and the present work*

The pattern formation in a granular plane Couette flow has attracted much attention during the last two decades using both simulation and theory (Hopkins & Louge 1991; Savage 1992; Tan & Goldhirsch 1997; Alam & Nott 1998; Conway & Glasser 2004; Sasvari, Kertesz & Wolf 2000; Alam *et al.* 2005; Alam & Luding 2005; Conway, Liu & Glasser 2006; Alam 2006; Gayen & Alam 2006; Khain & Meerson 2006; Khain 2007; Alam, Shukla & Luding 2008; Alam & Shukla 2008; Shukla & Alam 2009, 2011). The earliest particle-dynamics simulations of Hopkins & Louge (1991) identified travelling wave patterns in the form of oblique bands, aligned along the compressional axis of the shear flow, for a range of densities; most of these simulations were carried out with about 5000 particles and hence the observed structures were not so well defined. The 'large-scale' particle simulations of Tan & Goldhirsch (1997) at a particle volume fraction of 0.05 identified a variety of two-dimensional patterns, including a 'churn-type' flow. That the granular plane Couette flow supports inhomogeneous patterns, having modulations along both the streamwise and gradient directions, was predicted by Alam & Nott (1998) from a linear stability analysis of the pertinent continuum equations; they also systematically probed the effects of boundary conditions on the predicted instabilities. The structures of theoretically predicted (travelling and stationary) patterns look qualitatively similar to those observed in simulations (Hopkins & Louge 1991; Tan & Goldhirsch 1997).

Recently, Conway & Glasser (2004) have conducted a series of two-dimensional particle simulations of the bounded plane Couette flow at low-to-moderate densities (particle volume fraction less than 0.4 in two-dimensions), with walls acting as sinks of granular energy, which is one of the three cases considered by Alam & Nott (1998). In these simulations, the width and the length of the channel were

systematically varied so as to get access to any long-wave instability with streamwise modulations. They reproduced the main features of the full phase diagram of different instabilities as predicted by the linear stability analysis of Alam & Nott (1998). However, some of the long-wave instabilities of Alam & Nott (1998) were not found in simulations (Conway & Glasser 2004). Possibly those very long-wave instabilities are not admitted once the nonlinear terms are taken into account or the channel length of simulations was not long enough to capture structures with very large wavelengths. More recent dense simulations of Conway *et al.* (2006) identified a two-dimensional antisymmetric stationary wave (i.e. a sinuous-type mode), with significant modulations along the streamwise direction, which was found to be stable over millions of particle collisions. A nonlinear analysis of two-dimensional instabilities ($k_x \neq 0$, where k_x is the wavenumber along the periodic streamwise direction) is required to find out whether the simulated patterns can be predicted by continuum theory.

1.2.1. *Previous work on order-parameter theory in the granular Couette flow*

The one-dimensional shear-banding patterns (Tan 1995; Sasvari *et al.* 2000; Alam & Luding 2003; Conway & Glasser 2004; Alam *et al.* 2005; Conway *et al.* 2006; Khain & Meerson 2006; Khain 2007) in the granular plane Couette flow, in which the uniform shear flow breaks itself into regions of high and low shear rates along the gradient direction, appear due to a bulk instability of the underlying streamwise-independent equations (Alam & Nott 1998; Alam *et al.* 2005, 2008). An order-parameter theory, using the Landau–Stuart equation, of such shear-banding instabilities has recently been developed (Shukla & Alam 2009, 2011). Starting with granular hydrodynamic equations, Shukla & Alam (2009, 2011) derived the Landau–Stuart equation for the shear-banding instabilities (for the first time in granular flows) via weakly nonlinear analyses. They employed both the direct method of centre manifold reduction (Shukla & Alam 2009) and the indirect method of amplitude expansion (Shukla & Alam 2011), and showed the equivalence between these two methods that result in the same expression for the first Landau coefficient, which is the leading-order nonlinear correction in the nonlinear stability analysis. From a detailed analysis of the Landau–Stuart equation, Shukla & Alam (2011) showed that there is a switchover in the hierarchy of pitchfork bifurcations with increasing mean density (volume fraction of particles): (i) 'bifurcation from infinity' in the Boltzmann limit ($\phi < \phi_c^l \sim 0.15$, where ϕ_c^l is the minimum density below which the uniform shear flow is linearly stable), (ii) 'subcritical' bifurcation over a small window of densities at low-to-moderate densities ($\phi_c^l < \phi < \phi_c^s \sim 0.2$), (iii) 'supercritical' bifurcation at moderate densities ($\phi_c^s < \phi < \phi_c^{s1} \sim 0.4$), (iv) 'subcritical' bifurcation in dense flows ($\phi_c^{s1} < \phi < \phi_c^{s2} \sim 0.55$) and finally (v) 'supercritical' bifurcation in the dense limit ($\phi > \phi_c^{s2}$). It has been aptly concluded (Shukla & Alam 2011) that the granular plane Couette flow is a 'microcosm' of pitchfork bifurcations.

The plethora of pitchfork bifurcations at different densities agrees qualitatively with previous particle-dynamics simulations of the granular plane Couette flow. For example, the dilute simulations of Tan (1995) identified shear-banding patterns at a particle volume fraction of 0.05 which agrees with our scenario (i). The recent simulations of Khain (2007) also identified shear bands as a subcritical bifurcation (and hence bistability) in the dense limit, which agrees with our scenario (iv), and he has also verified his observation from the solution of one-dimensional continuum equations using modified constitutive relations with viscosity divergence. The simulations of Conway *et al.* (2006) on high-shear granular plane Couette flows of

both monodisperse and bidisperse particles showed the existence of 'stable' symmetric and asymmetric shear bands (with the symmetry being about the spatial location of the shear band around the channel centreline) for a range of mean densities. Both the linear stability analysis (Alam & Nott 1998) and the order-parameter theory (Shukla & Alam 2011) predicted such symmetric and asymmetric modes that can be stable/unstable depending on the Couette gap. What was missing for a long time is some experimental evidence of shear bands in the 'rapid' shear regime of the plane Couette flow, which is hard to realize in Earth-bound experiments where gravity dominates. However, the recent experiments of Conway *et al.* (2006) in a circular Couette geometry have uncovered the existence of shear bands (at moderate densities) which was shown to be stable over the experimental time scales of about an hour. On the whole, the predictions of the order-parameter theory (Shukla & Alam 2011) agree qualitatively with results from both particle simulations and experiments, with regard to the formation of shear bands in a rapid granular plane Couette flow.

1.2.2. *Present work*

Given the reasonable success of our order-parameter theory to predict one-dimensional finite-amplitude shear-banding instabilities (Shukla & Alam 2009, 2011), it is worthwhile to probe the nonlinear stability of two-dimensional patterns that emerge due to the travelling and stationary instabilities in granular Couette flow using the Landau–Stuart order-parameter equation (1.3). Following the Stuart–Watson theory (Stuart 1960; Watson 1960; Reynolds & Potter 1967) and our previous work (Shukla & Alam 2011), the order-parameter theory for such spatially inhomogeneous patterns in the two-dimensional granular Couette flow is developed in this paper, which constitutes one of our major goals here. Note that Shukla & Alam (2009, 2011) considered only streamwise-independent flow, which is equivalent to the zero-wavenumber ($k_x = 0$) limit of the present problem. Another goal of this work is to understand the nonlinear saturation of two-dimensional ($k_x \neq 0$) patterns that arise from a variety of linear instability modes in the granular plane Couette flow. Along with two-dimensional 'stationary' patterns that lead to pitchfork bifurcations, we found Hopf/oscillatory bifurcations in this flow and identified the parameter regimes of both subcritical and supercritical bifurcations in each case. We found that the two-dimensional granular plane Couette flow is susceptible to a plethora of nonlinear resonances, the criteria for which are clearly identified from an analysis of modal equations at quadratic order.

The Navier–Stokes hydrodynamic equations and constitutive relations are described in § 2, along with the steady mean flow of the plane Couette flow. The amplitude expansion method and the modal equations at different orders are briefly discussed in §§ 3 and 3.1; we have identified two types of resonances that are discussed in § 3.2, along with their numerical evidence in § 6.3. Different measures of nonlinear stability in terms of the first Landau coefficient as well as the signatures of Hopf bifurcations are discussed in § 4. The spectral-based numerical method of our previous work (Shukla & Alam 2011) has been extended to the present two-dimensional problem as discussed briefly in § 5. Detailed numerical results on various stationary and travelling wave instabilities, their nonlinear saturation, possible occurrences of nonlinear resonances, effects of mean density, and Couette gap and restitution coefficients are discussed in §§ 6.1–6.5. A qualitative comparison of nonlinear patterns with previous molecular dynamics simulations of granular Couette flow is provided in § 6.6. The conclusions are given in § 7.

2. Governing equations

The balance equations for mass, momentum and granular (pseudo-thermal) energy, in the absence of gravity, are

$$\left(\frac{\partial}{\partial \overline{t}} + \overline{\boldsymbol{u}} \cdot \overline{\boldsymbol{\nabla}}\right) \overline{\varrho} = -\overline{\varrho}(\overline{\boldsymbol{\nabla}} \cdot \overline{\boldsymbol{u}}), \tag{2.1}$$

$$\overline{\varrho}\left(\frac{\partial}{\partial \overline{t}} + \overline{\boldsymbol{u}} \cdot \overline{\boldsymbol{\nabla}}\right) \overline{\boldsymbol{u}} = -\overline{\boldsymbol{\nabla}} \cdot \overline{\boldsymbol{\Sigma}}, \tag{2.2}$$

$$\frac{\dim}{2}\overline{\varrho}\left(\frac{\partial}{\partial \overline{t}} + \overline{\boldsymbol{u}} \cdot \overline{\boldsymbol{\nabla}}\right) \overline{T} = -\overline{\boldsymbol{\nabla}} \cdot \overline{\boldsymbol{q}} - \overline{\boldsymbol{\Sigma}} : \overline{\boldsymbol{\nabla}}\overline{\boldsymbol{u}} - \overline{\mathscr{D}}, \tag{2.3}$$

respectively. Here $\overline{\varrho} = \overline{m}\,\overline{n} = \overline{\rho}\phi$ is the mass density, with $\overline{m}$, $\overline{n}$, $\overline{\rho}$, ϕ being the particle mass, the number density, the material density and the volume fraction of particles, respectively; $\overline{\boldsymbol{u}}$ is the bulk velocity (coarse-grained velocity field) and $\overline{T}$ is the granular temperature that measures the fluctuation kinetic energy of particles; $\overline{\boldsymbol{\Sigma}}$ is the stress tensor, $\overline{\boldsymbol{q}}$ is the flux of pseudo-thermal energy and $\overline{\mathscr{D}}$ denotes the rate of dissipation of energy per unit volume (granular energy). Here, the 'overbar' denotes the dimensional variables and 'dim' is the dimension of the problem (i.e. 2 for disks and 3 for spheres).

2.1. *Constitutive relations*

At Navier–Stokes order, the stress tensor is defined by the Newtonian form and the flux of granular (pseudo-thermal) energy by Fourier's law:

$$\overline{\boldsymbol{\Sigma}} = \left(\overline{p} - \overline{\zeta}(\overline{\boldsymbol{\nabla}} \cdot \overline{\boldsymbol{u}})\right)\boldsymbol{I} - 2\overline{\mu}\overline{\boldsymbol{S}}, \tag{2.4}$$

$$\overline{\boldsymbol{q}} = -\overline{\kappa}\overline{\boldsymbol{\nabla}}\,\overline{T}, \tag{2.5}$$

where $\overline{p}$ is the pressure, $\overline{\kappa}$ is the thermal conductivity, $\overline{\mu}$ and $\overline{\zeta}$ are the coefficients of shear and bulk viscosities, respectively, and $\overline{\boldsymbol{S}} = \left(\overline{\boldsymbol{\nabla}}\overline{\boldsymbol{u}} + (\overline{\boldsymbol{\nabla}}\overline{\boldsymbol{u}})^{\mathrm{T}}\right)/2 - (\overline{\boldsymbol{\nabla}} \cdot \overline{\boldsymbol{u}})\boldsymbol{I}/\dim$ is the deviatoric strain-rate tensor. The transport coefficients are

$$\left.\begin{aligned}
\overline{p}(\phi, \overline{T}) &= \overline{\rho}\overline{T}\,f_1(\phi), & \overline{\mu}(\phi, \overline{T}) &= \overline{\rho}\,\overline{d}\,\overline{T}^{1/2}\,f_2(\phi), \\
\overline{\zeta}(\phi, \overline{T}) &= \overline{\rho}\,\overline{d}\,\overline{T}^{1/2}\,f_3(\phi), & \overline{\kappa}(\phi, \overline{T}) &= \overline{\rho}\,\overline{d}\,\overline{T}^{1/2}\,f_4(\phi),
\end{aligned}\right\} \tag{2.6}$$

and the rate of collisional dissipation per unit volume is

$$\overline{\mathscr{D}}(\phi, \overline{T}) = \frac{\overline{\rho}}{\overline{d}}\overline{T}^{3/2}\,f_5(\phi, e), \tag{2.7}$$

where $\overline{d}$ is the diameter of a particle, e is the normal restitution coefficient, and $f_i(.)$ are the non-dimensional functions of particle volume fraction:

$$\left.\begin{aligned}
f_1(\phi) &= \phi(1 + 4\phi\chi), & f_2(\phi) &= \frac{5\sqrt{\pi}}{96\chi}\left(1 + \frac{8}{5}\phi\chi\right)^2 + \frac{8}{5\sqrt{\pi}}\phi^2\chi, \\
f_3(\phi) &= \frac{8}{3\sqrt{\pi}}\phi^2\chi, & f_4(\phi) &= \frac{25\sqrt{\pi}}{128\chi}\left(1 + \frac{12}{5}\phi\chi\right)^2 + \frac{4}{\sqrt{\pi}}\phi^2\chi, \\
f_5(\phi, e) &= \frac{12}{\sqrt{\pi}}(1 - e^2)\phi^2\chi.
\end{aligned}\right\} \tag{2.8}$$

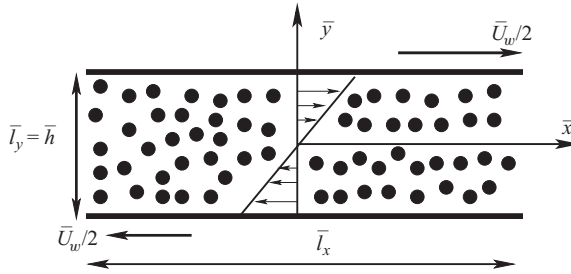In the above expressions, $\chi(\phi)$ is the contact radial distribution function, which is

FIGURE 1. Schematic of the planar shear flow of granular materials. In Cartesian coordinates, $\bar{x}$ and $\bar{y}$ represent the streamwise (flow) and tranverse (gradient) directions, respectively. The gap between two walls is $\bar{l}_y \equiv \bar{h}$ and the channel length is $\bar{l}_x$; the particles are of the same diameter $\bar{d}$ and material density $\bar{\rho}$.

chosen to be

$$\chi(\phi) = \frac{1}{1 - (\phi/\phi_m)^{1/3}}, \qquad (2.9)$$

where ϕ_m is the maximum volume fraction at random close packing. In continuation of our previous work on the nonlinear shear-banding instability (Shukla & Alam 2011), we will present results with (2.9); a different choice of $\chi(\phi)$ of the form

$$\chi(\phi) = \frac{(1 - \phi/2)}{(1 - \phi/\phi_m)^3} \qquad (2.10)$$

was tested, which did not yield any new instability in the granular plane Couette flow. Note that with $\phi_m = 1$, (2.10) simplifies to the well-known Carnahan–Starling form of the radial distribution function for spheres.

The choice of the above constitutive model, which is strictly valid in the quasi-elastic limit ($e \to 1$), has been discussed in our previous paper (Shukla & Alam 2011). It may be noted that the recent works on the kinetic theory of granular fluids (Sela & Goldhirsch 1998; Brilliantov & Pöschel 2004) have identified additional terms in the constitutive relations for the heat flux $\boldsymbol{q}$ and the collisional dissipation $\mathscr{D}$ at Navier–Stokes order: (i) a 'Dufour-like' term ($\propto \nabla\phi$) in (2.5) and (ii) a 'dilatational' term ($\sim \nabla \cdot \boldsymbol{u}$) in (2.7). While the effect of the additional 'dilatational' term in $\mathscr{D}$ was not tested, the effect of the 'Dufour-like' term in $\boldsymbol{q}$ was tested on the linear stability of bounded and unbounded plane shear flows (Alam & Nott 1998; Gayen & Alam 2006; Alam *et al.* 2008) but yielded no new instability mode.

2.2. *Non-dimensional equations and the steady mean flow*

We consider the plane shear flow of granular materials between two oppositely moving parallel walls with speed $\overline{U}_w/2$, as shown schematically in figure 1. We assume that the flow is 'two-dimensional' with $\bar{x}$ and $\bar{y}$ being the streamwise/flow and transverse/gradient directions, respectively, having no variations along the spanwise direction (i.e. $\bar{z}$-direction, which is normal to the flow-gradient plane). The analysis holds both for the plane shear flow of inelastic hard disks and for inelastic hard spheres in a box having a shallow depth such that the hydrodynamic fields are uniform along the spanwise direction.

For non-dimensionalization, we are using the gap between the two walls as the reference length ($\bar{h}$), the difference between the wall velocities as the reference velocity ($\overline{U}_w$), the inverse of the overall shear rate as the time scale ($\bar{h}/\overline{U}_w$) and the material density of particles as the density scale ($\bar{\rho}$); the scale for granular temperature is

$\overline{U}_w^2(\overline{d}/\overline{h})^2$. The stress tensor (2.4), the granular heat flux (2.5) and the collisional dissipation (2.7) have been non-dimensionalized by using $\overline{\rho}\,\overline{U}_w^2(\overline{d}/\overline{h})^2$, $\overline{\rho}\,\overline{U}_w^3(\overline{d}/\overline{h})^3$ and $(\overline{\rho}/\overline{d})\overline{U}_w^3(\overline{d}/\overline{h})^3$, respectively. With this scaling, the dimensionless balance equations for two-dimensional granular flows are

$$\frac{\partial \phi}{\partial t} + \frac{\partial}{\partial x}(\phi u) + \frac{\partial}{\partial y}(\phi v) = 0, \tag{2.11}$$

$$\phi \left[\frac{\partial}{\partial t} + u\frac{\partial}{\partial x} + v\frac{\partial}{\partial y} \right] u = -\frac{1}{H^2}\frac{\partial p}{\partial x} + \frac{1}{H^2}\frac{\partial}{\partial x}\left[2\mu\frac{\partial u}{\partial x} + \lambda\left(\frac{\partial u}{\partial x} + \frac{\partial v}{\partial y}\right) \right]$$
$$+ \frac{1}{H^2}\frac{\partial}{\partial y}\left[\mu\left(\frac{\partial u}{\partial y} + \frac{\partial v}{\partial x}\right) \right], \tag{2.12}$$

$$\phi \left[\frac{\partial}{\partial t} + u\frac{\partial}{\partial x} + v\frac{\partial}{\partial y} \right] v = -\frac{1}{H^2}\frac{\partial p}{\partial y} + \frac{1}{H^2}\frac{\partial}{\partial y}\left[2\mu\frac{\partial v}{\partial y} + \lambda\left(\frac{\partial u}{\partial x} + \frac{\partial v}{\partial y}\right) \right]$$
$$+ \frac{1}{H^2}\frac{\partial}{\partial x}\left[\mu\left(\frac{\partial u}{\partial y} + \frac{\partial v}{\partial x}\right) \right], \tag{2.13}$$

$$\frac{\dim}{2}\phi \left[\frac{\partial}{\partial t} + u\frac{\partial}{\partial x} + v\frac{\partial}{\partial y} \right] T = \frac{1}{H^2}\left[\frac{\partial}{\partial x}\left(\kappa\frac{\partial T}{\partial x}\right) + \frac{\partial}{\partial y}\left(\kappa\frac{\partial T}{\partial y}\right) \right]$$
$$- p(\nabla \cdot \boldsymbol{u}) + 2\mu\left[\left(\frac{\partial u}{\partial x}\right)^2 + \left(\frac{\partial v}{\partial y}\right)^2 \right]$$
$$+ \frac{1}{2}\left(\frac{\partial u}{\partial y} + \frac{\partial v}{\partial x}\right)^2 + \frac{\lambda}{2\mu}(\nabla \cdot \boldsymbol{u})^2 \right] - \mathscr{D}, \tag{2.14}$$

with dimensionless constitutive relations as

$$\left.\begin{array}{ll} p(\phi, T) = f_1 T, & \mu(\phi, T) = f_2\sqrt{T}, \quad \zeta(\phi, T) = f_3\sqrt{T}, \\[2mm] \lambda(\phi, T) = \left(\zeta - \dfrac{2}{\dim}\mu\right), & \kappa(\phi, T) = f_4\sqrt{T}, \quad \mathscr{D}(\phi, T) = f_5 T^{3/2}. \end{array}\right\} \tag{2.15}$$

In the above, $H = \overline{h}/\overline{d}$ is the ratio between the wall separation and the particle diameter, hereafter called the scaled Couette gap. In our previous papers (Shukla & Alam 2009, 2011), we considered one-dimensional streamwise-independent equations which can be obtained by putting $\partial/\partial x(\cdot) = 0$ in (2.11)–(2.14) since our focus was on the shear-banding instability, for which the associated patterns have no variations along the streamwise direction.

As in our previous work (Shukla & Alam 2009, 2011), we are imposing no-slip and zero heat-flux conditions at walls:

$$u = \pm 1/2, \quad v = 0, \quad \frac{\mathrm{d}T}{\mathrm{d}y} = 0, \quad \text{at} \quad y = \pm 1/2, \tag{2.16}$$

which is, of course, an idealization of the reality. Nevertheless, probing instability with such ideal boundary conditions helps to make a bridge with instabilities in a plane Couette flow with slip velocity and non-zero heat flux boundary conditions as established previously by Alam & Nott (1998) in the context of linear stability analysis.

The steady, fully developed equations with boundary conditions (2.16) admit the uniform shear solution:

$$u^0(y) = y, \quad v^0(y) = 0, \quad \phi^0 = \text{const.}, \quad T^0 = \frac{f_2(\phi^0)}{f_5(\phi^0, e)}, \tag{2.17}$$

for which the shear rate $(\mathrm{d}u^0/\mathrm{d}y = 1)$ is uniform/constant, with density and granular temperature being constants. The linear stability of (2.17) against two-dimensional perturbations has been investigated in detail by Alam & Nott (1998). In the present paper, we focus on nonlinear saturation of various linear instability modes using the Landau–Stuart equation which is derived in the following section for spatially periodic patterns.

3. Nonlinear stability: Landau–Stuart equation and resonance

In linear theory, we perturb the mean flow with infinitesimal perturbations and seek a solution of linearized perturbed equations in terms of Fourier modes

$$X(x, y, t) = X^0(y) + X'(x, y, t), \tag{3.1}$$

$$X'(x, y, t) = \hat{X}(y)\, \mathrm{e}^{(a+\mathrm{i}\omega)t}\, \mathrm{e}^{\mathrm{i}k_x x} = \hat{X}(y)\, \mathrm{e}^{at}\, \mathrm{e}^{\mathrm{i}(k_x x + \omega t)}, \tag{3.2}$$

and the latter (3.2) is possible since the linearized equations are invariant under translation in x and t. Here, $X^0 = (\phi^0, u^0, v^0, T^0)$ is the steady mean flow (2.17), $\hat{X} = (\hat{\phi}, \hat{u}, \hat{v}, \hat{T})$ is the modal amplitude of perturbation, k_x is the wavenumber along the streamwise direction, a and ω are the growth rate and frequency of the perturbation, respectively. The flow is stable (or unstable) according to linear theory if a is negative (or positive) and neutrally stable if $a = 0$. The above solution is valid as long as the perturbation amplitude is infinitesimally small $(|X'/X^0| \ll 1)$, so that we can neglect the nonlinear terms. For 'finite' amplitude perturbations, the nonlinear terms are important and an amplitude equation is required to predict the behaviour of the flow. Shukla & Alam (2011) followed the amplitude expansion method (Stuart 1960; Watson 1960; Reynolds & Potter 1967) to develop an order-parameter theory for the nonlinear shear-banding instability $(k_x = 0)$ of a granular plane Couette flow. The same order-parameter theory is extended to two-dimensional disturbances $(k_x \neq 0)$ in this work.

We start with the nonlinear disturbance equations, which can be represented in matrix form

$$\left(\frac{\partial}{\partial t} - \mathcal{L}\right) X' = \mathcal{N}_2(X', X'; \partial_t) + \mathcal{N}_3(X', X', X'), \tag{3.3}$$

where

$$\mathcal{L} \equiv \mathcal{L}\left(\frac{\partial}{\partial x}, \frac{\partial^2}{\partial x^2}, \frac{\partial}{\partial y}, \frac{\partial^2}{\partial y^2}; \phi^0, \dots\right) \tag{3.4}$$

is the linear stability operator, $\mathcal{N}_2$ and $\mathcal{N}_3$ are the quadratic and cubic nonlinear terms, respectively, of state variables X' and their spatial derivatives. The explicit expressions of $\mathcal{L}$ and the nonlinear terms $\mathcal{N}_2$ and $\mathcal{N}_3$ are omitted for the sake of brevity. The argument ∂_t in $\mathcal{N}_2(X', X'; \partial_t)$ refers to the fact that there are quadratic nonlinearities that involve time derivatives of the form $\phi' \partial(u', v', T')/\partial t$ (in momentum and granular energy equations) and this is a consequence of the fact that the granular fluid is compressible. All nonlinear terms are accumulated by Taylor expansion of each transport coefficient around the base state (ϕ^0, T^0), and retaining terms that are up to cubic order in perturbation amplitude as detailed in Shukla & Alam (2011). In the following, we provide a brief account of the nonlinear theory, mainly

pointing out the essential differences from our previous work (Shukla & Alam 2011) as well as deriving the criteria for possible nonlinear resonances at quadratic order in amplitude. It may be noted that the present nonlinear equations agree with those in Shukla & Alam (2011) for the special case of streamwise-independent perturbations ($k_x = 0$).

Let $A(t)$ be the real amplitude of the finite-size disturbance and let $\omega(A)$ be its frequency, which is allowed to depend on A in nonlinear theory. Now all phase information of the disturbance (see (3.2)) is incorporated into a new variable θ via the following transformation (Reynolds & Potter 1967):

$$\theta = k_x x + \omega t, \quad \omega = \omega(A), \quad A = A(t), \quad y = y. \tag{3.5}$$

Using (3.5), the time and spatial derivatives are transformed according to

$$\frac{\partial}{\partial t} \rightarrow \frac{\mathrm{d}A}{\mathrm{d}t}\frac{\partial}{\partial A} + \left[\omega + \frac{\mathrm{d}\omega}{\mathrm{d}A}\left(t\frac{\mathrm{d}A}{\mathrm{d}t}\right)\right]\frac{\partial}{\partial\theta}, \tag{3.6a}$$

$$\left(\frac{\partial}{\partial x}, \frac{\partial^2}{\partial x^2}\right) \rightarrow \left(k_x\frac{\partial}{\partial\theta}, k_x^2\frac{\partial^2}{\partial\theta^2}\right), \tag{3.6b}$$

$$\left(\frac{\partial}{\partial y}, \frac{\partial^2}{\partial y^2}\right) \rightarrow \left(\frac{\partial}{\partial y}, \frac{\partial^2}{\partial y^2}\right). \tag{3.6c}$$

Since the perturbation amplitude $A(t)$ is assumed to be a slowly varying function of time, the first and second terms on the right-hand side in (3.6a) represent *slow* and *fast* time scales, respectively. On the whole, the above transformation (3.5) embodies a *two time-scale* ansatz.

Substituting (3.6a), (3.6b) and (3.6c) into (3.3) we transform the nonlinear equations (3.3) from the (x, y, t)-plane to (A, θ, y)-plane:

$$\left[\mathcal{M}(\partial_A, \partial_\theta; \omega) - \mathcal{L}\left(k_x\partial_\theta, k_x^2\partial_\theta^2, \partial_y, \partial_y^2; \phi^0, \dots\right)\right] X' = \mathcal{N}_2(X', X'; \partial_t) + \mathcal{N}_3(X', X', X'), \tag{3.7}$$

where

$$\mathcal{L}(\cdot) \equiv \mathcal{L}\left(k_x\frac{\partial}{\partial\theta}, k_x^2\frac{\partial^2}{\partial\theta^2}, \frac{\partial}{\partial y}, \frac{\partial^2}{\partial y^2}; \phi^0, \dots\right), \tag{3.8a}$$

$$\mathcal{M} = \left[\frac{\mathrm{d}A}{\mathrm{d}t}\frac{\partial}{\partial A} + \left(\omega + \frac{\mathrm{d}\omega}{\mathrm{d}A}\left(t\frac{\mathrm{d}A}{\mathrm{d}t}\right)\right)\frac{\partial}{\partial\theta}\right]\boldsymbol{I} \tag{3.8b}$$

are the linear stability operator and a diagonal operator, respectively, with $\boldsymbol{I}$ being the identity operator.

The coefficients of transformed disturbance equations (3.7) and boundary conditions do not depend explicitly on θ, which implies that (3.7) is translation invariant in θ. This leads us to assume a solution for disturbance variables in terms of a Fourier series in θ,

$$X'(x, y, t) \equiv X'(A, \theta, y) = \sum_{k=-\infty}^{\infty} X^{(k)}(A(t), y)\,\mathrm{e}^{\mathrm{i}k\theta}, \tag{3.9}$$

where the superscript k represents a particular Fourier mode, $X^{(-k)} = \tilde{X}^{(k)}$ and the 'tilde' denotes a complex conjugate quantity. Substituting (3.9) into (3.7) and equating the coefficients of $\mathrm{e}^{\mathrm{i}k\theta}$, we obtain a set of partial differential equations for $X^{(k)}$, with $k = 1, 2, \dots$. For example, the continuity equation (first equation in (3.7)) gets

transformed into

$$\frac{\mathrm{d}A}{\mathrm{d}t}\frac{\partial \phi^{(k)}}{\partial A} + \left[\omega + \frac{\mathrm{d}\omega}{\mathrm{d}A}\left(t\frac{\mathrm{d}A}{\mathrm{d}t}\right)\right]\frac{\partial \phi^{(k)}}{\partial \theta} + ikk_x u^0 \phi^{(k)} + ikk_x \phi^0 u^{(k)}$$

$$+ \left(\phi_y^0 + \phi^0 \frac{\partial}{\partial y}\right) v^{(k)} = \text{NL terms.} \quad (3.10)$$

Note that the steady terms $O(1)$ represent the mean flow (ϕ^0, u^0, v^0, T^0), $O(A)$ terms give the linear problem, and $O(A^2)$ terms represent the harmonics of the fundamental and the leading-order distortion of the mean flow. This suggests the following separation of variables solution in terms of a power series in perturbation amplitude:

$$X^{(k)}(A(t), y) = \sum_{n \geqslant k} A^n(t) X^{[k;n]}(y), \quad (3.11)$$

where the 'dual index' in superscripts $[k;n]$ is applied such that the first index $k \geqslant 0$ refers to a particular mode and the second index $n \geqslant 1$ refers to the order of a particular term $O(A^n)$. Here, $X^{(1;1)}$ is the fundamental mode which is $O(A)$, and $X^{[0;n]}$ is the distortion of the mean flow which is $O(A^n)$.

Since the perturbation amplitude $A(t)$ must be proportional to e^{at} as $A \to 0$ (the limit of infinitesimal disturbances of linear theory), we can write power-series expansions for

$$A^{-1}\frac{\mathrm{d}A}{\mathrm{d}t} = \sum_{n \geqslant 0} a^{(n)} A^n, \quad (3.12)$$

$$\frac{\mathrm{d}\theta}{\mathrm{d}t} \equiv \omega + \frac{\mathrm{d}\omega}{\mathrm{d}A}\left(t\frac{\mathrm{d}A}{\mathrm{d}t}\right) = \sum_{n \geqslant 0} b^{(n)} A^n. \quad (3.13)$$

Note that the leading terms of (3.12) and (3.13) constitute the eigenvalue, $a^{(0)} + ib^{(0)}$, of the linear stability operator. Equations (3.11)–(3.13) are of the same type as are all expansions in small perturbation amplitude A, and this is why the Stuart–Watson theory is termed the 'amplitude expansion method'.

Substituting (3.11)–(3.13) into (3.10) and equating the coefficients of A^n, we obtain

$$(na^{(0)} + ikb^{(0)})\phi^{[k;n]} + ikk_x(u^0 \phi^{[k;n]} + \phi^0 u^{[k;n]}) + \left(\phi_y^0 + \phi^0 \frac{\partial}{\partial y}\right) v^{[k;n]}$$

$$= -(a^{[n-1]} + ib^{[n-1]})\phi^{[1;1]}\delta_{k1} - (ma^{[n-m]} + ikb^{[n-m]})\phi^{\{k;m\}} + \text{NL terms,} \quad (3.14)$$

where δ_{k1} is the Kronecker delta. In the above, we have used the following superscript summation notations in terms of three brackets:

$$(j) \Rightarrow j \geqslant 0, \quad [j] \Rightarrow j \geqslant 1 \quad \text{and} \quad \{j\} \Rightarrow j \geqslant 2. \quad (3.15)$$

When these brackets, $(\cdot)$, $[\cdot]$ and $\{\cdot\}$, are applied to the dual-index notation such as $k;n$, the above definition (3.15) holds for the second index n. Similarly, we can represent x-momentum, y-momentum and energy equations in the form (3.14). This leads to a sequence of linear inhomogeneous ordinary differential equations at each order in perturbation amplitude $O(A^n)$, the matrix equivalent of which can be written in operator form:

$$\boldsymbol{L}_{kn} X^{[k;n]} = -c^{[n-1]} X^{[1;1]}\delta_{k1} + G_{kn}, \quad (3.16)$$

where $X^{[k;n]} = (\phi^{[k;n]}, u^{[k;n]}, v^{[k;n]}, T^{[k;n]})^{\mathrm{T}}$ is the disturbance vector,

$$c^{[n-1]} = a^{[n-1]} + \mathrm{i}b^{[n-1]}, \tag{3.17a}$$

$$G_{kn} = -\left(ma^{[n-m]} + \mathrm{i}kb^{[n-m]}\right)X^{\{k;m\}} + E_{kn}/(1 + \delta_{0k}) + F_{kn}, \tag{3.17b}$$

$$\boldsymbol{L}_{kn} = \left(na^{(0)} + \mathrm{i}kb^{(0)}\right)\boldsymbol{I} - \boldsymbol{L}_k \tag{3.17c}$$

are the Landau coefficients, nonlinear vector, and linear operator, respectively, and

$$\boldsymbol{L}_k \equiv \mathscr{L}\left(\mathrm{i}kk_x, (\mathrm{i}kk_x)^2, \frac{\mathrm{d}}{\mathrm{d}y}, \frac{\mathrm{d}^2}{\mathrm{d}y^2}; \phi^0, \dots\right) \tag{3.18}$$

is the linear operator for the kth Fourier mode, with $\boldsymbol{L}_{k=1}$ being the well-known linear stability operator. It can be verified that $X^{[k;n]} = 0$, when $k + n$ is odd and hence $c^{[n]}$ vanishes for odd n. Note that the nonlinear terms $E_{kn} \equiv E_{kn}(X, X)$ and $F_{kn} \equiv F_{kn}(X, X, X)$ have quadratic and cubic nonlinearities, respectively. It is worth pointing out that the cubic nonlinearities must be retained in disturbance equations (3.7) for correct computation of the first Landau coefficient $c^{(2)}$.

The above system (3.16) needs to be solved at each order of amplitude along with boundary conditions:

$$u^{[k;n]} = 0, \quad v^{[k;n]} = 0, \quad \frac{\mathrm{d}T^{[k;n]}}{\mathrm{d}y} = 0. \tag{3.19}$$

3.1. First Landau coefficient, solvability condition and higher harmonics

At cubic order $O(A^3)$, we get an equation for the distortion to the fundamental mode $X^{[1;3]}$ by substituting $k = 1$ and $n = 3$ into (3.16):

$$\boldsymbol{L}_{13}X^{[1;3]} \equiv \left[\left(3a^{(0)} + \mathrm{i}b^{(0)}\right)\boldsymbol{I} - \boldsymbol{L}_1\right]X^{[1;3]} = -c^{[2]}X^{[1;1]} + G_{13}, \tag{3.20}$$

where $c^{(2)}$ is the first Landau coefficient that needs to be determined. The dependence of G_{13} on modal amplitudes $X^{[i;j]}$ is given by

$$\begin{aligned}
G_{13} = {}& N_2(X^{[0,2]}, X^{[1;1]}) + N_2(X^{[1;1]}, X^{[0,2]}) + N_2(\tilde{X}^{[1,1]}, X^{[2;2]}) \\
&+ N_2(X^{[2;2]}, \tilde{X}^{[1,1]}) + N_3(\tilde{X}^{[1,1]}, X^{[1;1]}, X^{[1;1]}) \\
&+ N_3(X^{[1;1]}, \tilde{X}^{[1,1]}, X^{[1;1]}) + N_3(X^{[1;1]}, X^{[1;1]}, \tilde{X}^{[1,1]}).
\end{aligned} \tag{3.21}$$

This nonlinear vector is completely known since $X^{[1;1]}$, $X^{[2;2]}$ and $X^{[0,2]}$ can be found by solving the following set of equations sequentially:

$$\boldsymbol{L}_{11}X^{[1;1]} \equiv \left[(a^{(0)} + \mathrm{i}b^{(0)})\boldsymbol{I} - \boldsymbol{L}_1\right]X^{[1;1]} = 0, \tag{3.22}$$

$$\boldsymbol{L}_{22}X^{[2;2]} \equiv \left[2(a^{(0)} + \mathrm{i}b^{(0)})\boldsymbol{I} - \boldsymbol{L}_2\right]X^{[2;2]} = N_2(X^{[1;1]}, X^{[1;1]}), \tag{3.23}$$

$$\boldsymbol{L}_{02}X^{[0;2]} \equiv \left[2a^{(0)}\boldsymbol{I} - \boldsymbol{L}_0\right]X^{[0;2]} = N_2(\tilde{X}^{[1;1]}, X^{[1;1]}) + N_2(X^{[1;1]}, \tilde{X}^{[1;1]}), \tag{3.24}$$

where the linear operators $\boldsymbol{L}_0$, $\boldsymbol{L}_1$ and $\boldsymbol{L}_2$ can be easily obtained from (3.18). It is worth pointing out that $\boldsymbol{L}_0$ is simply the linear stability operator for streamwise-independent or shear-banding ($k_x = 0$) modes. While the second harmonic $X^{[2;2]}$ is, in general, a complex quantity, the mean-flow distortion $X^{[0;2]}$ is always a real harmonic. For the special case of shear-banding modes ($k_x = 0$), it has been shown (Shukla & Alam 2011) that the second harmonic $X^{[2;2]}$ is real and $X^{[2;2]} = \tilde{X}^{[2;2]} = X^{[0;2]}$.

From (3.20), we note that when $a^{(0)} = 0$, $\boldsymbol{L}_{13}$ is identical to $\boldsymbol{L}_{11}$, for which the associated homogeneous problem and its adjoint (see below) have eigensolutions and hence the problem (3.20) is solvable if and only if the inhomogeneous part is

orthogonal to the adjoint eigenfunction. This is called the solvability condition, which simplifies to yield the expression for the first Landau coefficient:

$$c^{[2]} = a^{[2]} + ib^{[2]} = \frac{\langle X^\dagger, G_{13} \rangle}{\langle X^\dagger, X^{[1;1]} \rangle}, \tag{3.25}$$

with the inner product $\langle \cdot, \cdot \rangle$ for two complex-valued functions $f(y)$ and $g(y)$ being defined by

$$\langle f(y), g(y) \rangle = \int_{-1/2}^{1/2} \tilde{f}(y) g(y) \, \mathrm{d}y. \tag{3.26}$$

The adjoint eigenfunction $X^\dagger$ in (3.25) is obtained by solving the adjoint eigenvalue problem

$$\frac{\partial X^\dagger}{\partial t} = \mathscr{L}^\dagger X^\dagger, \tag{3.27}$$

with the adjoint operator $\mathscr{L}^\dagger$ being obtained from the following definition:

$$\langle X^\dagger, \mathscr{L} X \rangle = \langle \mathscr{L}^\dagger X^\dagger, X \rangle. \tag{3.28}$$

The explicit form of $\mathscr{L}^\dagger$ is omitted for the sake of brevity.

Once $c^{[2]}$ is determined from (3.25), the right-hand side of (3.20) is completely known since G_{13} is a function of $X^{[1;1]}$, $X^{[0;2]}$ and $X^{[2;2]}$ only as defined in (3.21), and hence we can solve (3.20) to yield the distortion to the fundamental mode $X^{[1;3]}$. The equation for the third harmonic $X^{[3;3]}$,

$$\boldsymbol{L}_{33} X^{[3;3]} \equiv \left[3(a^{(0)} + ib^{(0)})\boldsymbol{I} - \boldsymbol{L}_3 \right] X^{[1;3]} = G_{33}, \tag{3.29}$$

is also simultaneously solved since the nonlinear terms

$$G_{33} = N_2(X^{[1;1]}, X^{[2;2]}) + N_2(X^{[2;2]}, X^{[1;1]}) + N_3(X^{[1;1]}, X^{[1;1]}, X^{[1;1]}) \tag{3.30}$$

are known functions of the first and second harmonics. Knowing $X^{[1;1]}$, $X^{[2;2]}$, $X^{[0;2]}$, $X^{[1;3]}$ and $X^{[3;3]}$, we can calculate the nonlinear disturbance field up to cubic order as discussed in §4.3.

3.2. *Nonlinear resonance: criteria for mean-flow and 1 : 2 resonances*

The modal equations at quadratic order (3.24) and (3.23) admit two types of resonances: (i) mean-flow resonance and (ii) 1 : 2 resonance, which are analysed below. Since both appear at $O(A^2)$ we call them 'nonlinear' resonances, and this nomenclature distinguishes them from linear resonance, which occurs when two eigenvalues of the linear stability operator (3.22) are identical.

The system of equations for mean-flow distortion (3.24) is solvable, i.e.

$$X^{[0;2]} = \left[2a^{(0)}\boldsymbol{I} - \boldsymbol{L}_0 \right]^{-1} G_{02} = \text{finite}, \tag{3.31}$$

if the operator $(2a^{(0)}\boldsymbol{I} - \boldsymbol{L}_0)$ is non-singular; this is possible if and only if $2a^{(0)}$ is not equal to any of the eigenvalues of $\boldsymbol{L}_0$ (which is the linear stability operator for shear-banding modes $k_x = 0$). The violation of this condition is responsible for the resonance between a linear mode of the operator $\boldsymbol{L}_0$ (which is a shear-banding mode) and the mean-flow distortion $X^{[0;2]}$ at k_x, called the 'mean-flow resonance'. Therefore, the criterion for the mean-flow resonance can be written as

$$2a_{j_1}^{(0)}(k_x) = a_{j_2}^{(0)}(k_x = 0) \quad \text{and} \quad b_{j_2}^{(0)}(k_x = 0) = 0, \tag{3.32}$$

for two modes j_1 and j_2. Here $a_{j_1}^{(0)} = \text{Re}\{c_{j_1}^{(0)}\}$ is an eigenvalue of the linear stability operator $\boldsymbol{L}_1$ and $a_{j_2}^{(0)} \equiv c_{j_2}^{(0)}$ is an eigenvalue of the shear-banding operator $\boldsymbol{L}_0$.

Therefore, the interaction of a linear mode with a shear-banding mode, obeying (3.32), is responsible for the genesis of the 'mean-flow' resonance. We will show evidence of such resonance in §6.3.

The system of inhomogeneous equations for the second harmonic (3.23) has a solution, i.e.

$$X^{[2;2]} = \left[2c^{(0)} I - L_2\right]^{-1} G_{22} = \text{finite} \tag{3.33}$$

if and only if $2c^{(0)}$ is not equal to any of the eigenvalues of L_2. Recall from (3.18) that the second harmonic operator L_2 is simply the linear stability operator with wavenumber $2k_x$. Therefore, the solution for the second harmonic (3.33) becomes indeterminate when $2c^{(0)}$ (with $c^{(0)}$ being an eigenvalue of L_1) is an eigenvalue of L_2, leading to a resonance between two modes with their wavenumber ratio being $1:2$. This is referred to as '1:2 resonance', the criterion for which can be written as

$$2c_{j_1}^{(0)}(k_x) = c_{j_2}^{(0)}(2k_x),$$
$$\Rightarrow 2a_{j_1}^{(0)}(k_x) = a_{j_2}^{(0)}(2k_x) \quad \text{and} \quad 2b_{j_1}^{(0)}(k_x) = b_{j_2}^{(0)}(2k_x), \tag{3.34}$$

for any positive integers j_1 and j_2 that correspond to two different modes. It is clear from (3.18) that while $c_{j_1}^{(0)}(k_x)$ is an eigenvalue of L_1, $c_{j_2}^{(0)}(2k_x)$ is an eigenvalue of L_2. Therefore, the interaction of a fundamental mode with a second harmonic, obeying (3.34), is responsible for the genesis of $1:2$ resonance. We will discuss the possible occurrence of such resonance in §6.3.

In either type of resonances, $X^{[0;2]}$ or $X^{[2;2]}$ diverges and hence the first Landau coefficient (3.25), which is given in terms of an inner product of a nonlinear function G_{13}, would also diverge since G_{13} in (3.21) is a linear function of $X^{[0;2]}$ and $X^{[2;2]}$. Therefore, the signature of above resonances would appear as a discontinuity in the first Landau coefficient as we shall demonstrate in §6.3. It is worth pointing out that the mean-flow and $1:n$ resonances have been uncovered and are known to play an important role in dynamical transition and pattern formation, via mode interactions, for both Newtonian and non-Newtonian fluids in a variety of flows (Mizushima & Gotoh 1985; Knobloch & Proctor 1988; Proctor & Jones 1988; Manneville 1990; Fujimura 1992; Suslov & Paolucci 1997; Guba & Worster 2010).

4. Analysis of Landau–Stuart equation, bifurcation and disturbance field

From the viewpoint of nonlinear stability, the pertinent question is: do the unstable/stable 'linear' modes become stable/unstable if we disturb the flow with finite amplitude disturbances? Do we have supercritical or subcritical bifurcation in each case? The nonlinear terms may saturate the exponential growth of the disturbance for the bands of wavenumbers where the flow is linearly unstable due to travelling and stationary instabilities. What is the nature of nonlinear solutions? The above issues are systematically probed in §6 using the weakly nonlinear theory developed in §3. In the following, we briefly discuss different measures of nonlinear stability in terms of the equilibrium amplitude, the types of bifurcations (pitchfork or Hopf) and the nonlinear disturbance field.

4.1. *Equilibrium amplitude and phase velocity*

As in our previous work (Shukla & Alam 2009, 2011), we will restrict our attention to the leading nonlinear correction in the order-parameter theory, namely the computation of the first Landau coefficient $c^{(2)} = a^{(2)} + ib^{(2)}$ from (3.25). Knowing the growth rate $a^{(0)}$ and the real part of the first Landau coefficient $a^{(2)}$, the equilibrium

amplitude ($dA/dt = 0$) is calculated from (3.12) as

$$A_e = \pm\sqrt{-\frac{a^{(0)}}{a^{(2)}}}. \tag{4.1}$$

Clearly, the equilibrium solution exists if and only if $a^{(0)}$ and $a^{(2)}$ are of opposite signs. For linearly unstable flows, $a^{(0)} > 0$ and therefore $a^{(2)}$ must be negative for the existence of any equilibrium solution – the new stable solution bifurcates from the critical point, leading to supercritical bifurcations. On the other hand, the existence of any equilibrium solution for linearly stable [$a^{(0)} < 0$] flows requires a positive value of $a^{(2)}$, leading to subcritical bifurcations.

As explained in §3, the nonlinearities also affect the propagation speed of the disturbance: see (3.5) and (3.13). More specifically, the imaginary part of the first Landau coefficient, $b^{(2)}$, changes the equilibrium phase velocity c_{ph}^e, whose expression follows from (3.13):

$$c_{ph}^e = -\frac{\omega}{k_x} = c_{ph} - \frac{b^{(2)}A_e^2}{k_x}, \tag{4.2}$$

where A_e is given by (4.1), and c_{ph} represents the linear phase velocity,

$$c_{ph} = -\frac{b^{(0)}}{k_x}, \tag{4.3}$$

with $b^{(0)}$ being the imaginary part of the complex frequency $c^{(0)} = a^{(0)} + ib^{(0)}$. Note that $b^{(2)} = 0$ for a stationary instability, for which $c_{ph}^e = c_{ph} = 0$.

4.2. Bifurcations, limit cycle and spirals

Up to the cubic order in amplitude, the Landau–Stuart equations (3.12)–(3.13) simplify to

$$\frac{dA}{dt} = a^{(0)}A + a^{(2)}A^3, \tag{4.4}$$

$$\frac{d\theta}{dt} = b^{(0)} + b^{(2)}A^2. \tag{4.5}$$

For stationary disturbances, $b^{(n)} = 0$ for $n \geqslant 0$ and the phase equation (4.5) is identically satisfied, $\theta \equiv 0$. Hence, the normal form for pitchfork bifurcations is (4.4), for which the fixed points are simple as given by 0 and A_e in (4.1). In contrast to pitchfork bifurcations, for which the linear eigenvalue is real, a complex eigenvalue $c^{(0)} = a^{(0)} + ib^{(0)}$, representing an oscillatory mode, leads to oscillatory or Hopf bifurcation, for which the normal-form equations are (4.4)–(4.5), which we discuss below.

4.2.1. Case I: $a^{(2)} < 0$

For negative values of the first Landau coefficient ($a^{(2)} < 0$), we have three situations when (i) $a^{(0)} < 0$: the origin $A = 0$ is a stable spiral; (ii) $a^{(0)} = 0$: the origin is a stable spiral with algebraically fast decay; and (iii) $a^{(0)} > 0$ yields an unstable spiral at the origin and a stable limit cycle solution at $A = \sqrt{-a^{(0)}/a^{(2)}}$ via a supercritical Hopf bifurcation. All the above situations are schematically shown in figure 2(a–c). Figure 2(a) shows a state of a stable spiral at the origin for $a^{(0)} < 0$, which loses stability as the control parameter increases from its critical value (when $a^{(0)} = 0$) and gives a stable limit-cycle solution which is shown in figure 2(b). The supercritical bifurcation is shown in figure 2(c), where the stable (indicated by arrows) and unstable solutions are shown by solid and dashed lines, respectively.

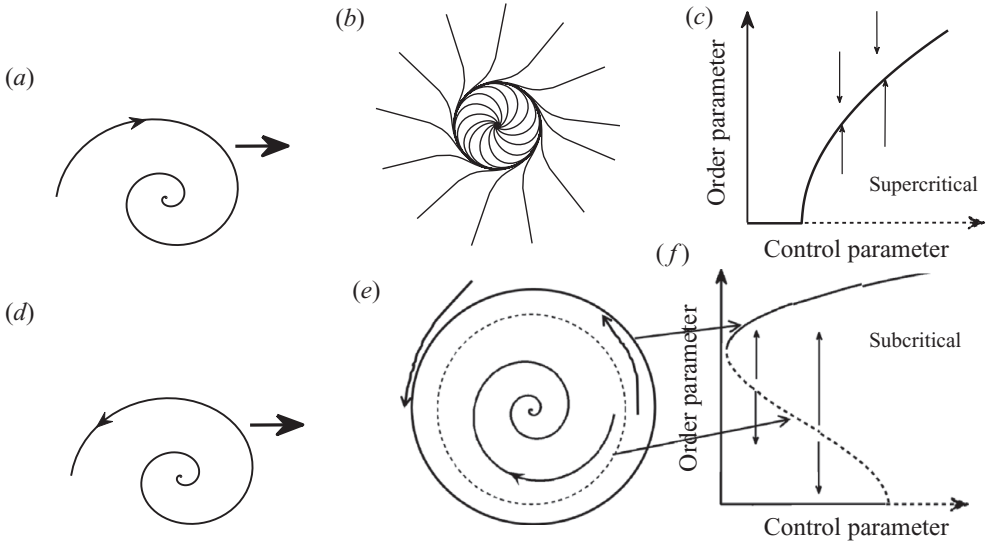FIGURE 2. Hopf bifurcation and solution trajectories: (a) $a^{(0)} < 0$ and $a^{(2)} < 0$, stable spiral; (b) $a^{(0)} > 0$ and $a^{(2)} < 0$, stable limit cycle; (c) supercritical bifurcation; (d) $a^{(0)} > 0$ and $a^{(2)} > 0$, unstable spiral; (e) $a^{(0)} < 0$ and $a^{(2)} > 0$, unstable limit cycle; (f) subcritical bifurcation.

4.2.2. *Case II: $a^{(2)} > 0$*

Similarly, for $a^{(2)} > 0$ we have two situations, $a^{(0)} > 0$ or $a^{(0)} < 0$. In the former case, we have an unstable spiral at the origin (see figure 2d). If $a^{(0)} < 0$, three solutions exist: a stable spiral at the origin, an unstable limit cycle at a distance $A = \sqrt{-a^{(0)}/a^{(2)}}$ and a stable limit cycle corresponding to the higher-amplitude branch. This higher-amplitude branch can be obtained by adding a stabilizing 'quintic' nonlinear term to the Landau–Stuart equation:

$$\frac{dA}{dt} = a^{(0)}A + a^{(2)}A^3 + a^{(4)}A^5. \tag{4.6}$$

This equation has five equilibrium solutions, a zero solution (base state or mean flow) and four non-trivial solutions, as defined by

$$|A_e| = \pm\sqrt{\frac{-a^{(2)} \pm \sqrt{(a^{(2)})^2 - 4a^{(0)}a^{(4)}}}{2a^{(4)}}}. \tag{4.7}$$

Among these four solutions, two are stable equilibrium solutions and the remaining two are unstable. Figure 2(f) shows the bifurcation diagram for subcritical instabilities, where the dotted line represents an unstable solution corresponding to an 'unstable' limit cycle (dashed circle in figure 2e). The solid line in figure 2(f) corresponds to the higher-order solution that represents a 'stable' limit cycle with a larger amplitude as shown by the outer circle in figure 2(e) – this solution corresponds to $a^{(0)} < 0$, $a^{(2)} > 0$ and $a^{(4)} < 0$ in (4.6). A disturbance with an amplitude greater than the amplitude of the stable limit cycle (outer circle in figure 2e) or an amplitude in between the outer limit cycle and the inner limit cycle will converge to the 'stable' outer limit cycle as shown by curved arrows in figure 2(e). If the amplitude of the disturbance is less than the amplitude of the inner (unstable) limit cycle in figure 2(e), the amplitude converges to the origin, which gives a stable spiral at the origin.

4.3. *Nonlinear disturbance field*

The nonlinear disturbance flow field $X'(x, y, t) = (\phi', u', v', T')(x, y, t)$, correct up to the cubic order in perturbation amplitude $O(A^3)$, can be written as

$$
\begin{aligned}
X'(x, y, t) &= A^2 X^{[0;2]} + \left[\left(A X^{[1;1]} e^{i\theta} + A^3 X^{[1;3]} e^{i\theta} + A^2 X^{[2;2]} e^{2i\theta} + A^3 X^{[3;3]} e^{3i\theta} \right) + \text{c.c.} \right] \\
&= A^2 X^{[0;2]} + 2A \left[X_r^{[1;1]} \cos(\theta) - X_i^{[1;1]} \sin(\theta) \right] \\
&\quad + 2A^3 \left[X_r^{[1;3]} \cos(\theta) - X_i^{[1;3]} \sin(\theta) \right] + 2A^2 \left[X_r^{[2;2]} \cos(2\theta) - X_i^{[2;2]} \sin(2\theta) \right] \\
&\quad + 2A^3 \left[X_r^{[3;3]} \cos(3\theta) - X_i^{[3;3]} \sin(3\theta) \right].
\end{aligned}
\tag{4.8}
$$

Here the subscripts r and i refer to the real and imaginary parts of the complex vector $X^{[i;j]}$, and $\theta = (k_x x + \omega t)$. Note that $X^{[0;2]}$ is the distortion of the mean flow (that appears at $O(A^2)$), which is always real. At equilibrium $(\mathrm{d}A/\mathrm{d}t = 0)$, (3.12) leads to $\omega = (b^{(0)} + b^{(2)} A^2)$, and hence the expression for θ is

$$
\theta = k_x x + \left(b^{(0)} + b^{(2)} A^2 \right) t = k_x \left(x - c_{ph}^e t \right),
\tag{4.9}
$$

with c_{ph}^e being given by (4.2).

Knowing the equilibrium amplitude (4.1) and the phase velocity (4.2), now we can calculate the nonlinear disturbance flow field from (4.8) and (4.9) by using the numerical solutions for $X^{[1;1]}$, $X^{[0;2]}$, $X^{[2;2]}$, $X^{[1;3]}$ and $X^{[3;3]}$ that are obtained from (3.22), (3.24), (3.23), (3.20) and (3.29), respectively. In §6, we will a make comparison between the linear $(O(A))$ and nonlinear $(O(A^3))$ disturbance fields in the (x, y)-plane.

5. Numerical method and control parameters

In our previous work (Shukla & Alam 2011), a spectral-based numerical method has been developed to solve (3.22), (3.24), (3.23), (3.20), (3.25) and (3.29) for the special case of shear-banding instability $k_x = 0$. The same numerical technique has been extended to the present problem with $k_x \neq 0$; there is no change in the methodology of the numerical technique, rather we needed to incorporate additional terms, which depend on k_x, in the numerical code. In short, we have discretized all the differential equations (linear and nonlinear) by spectral collocation techniques using Chebyshev polynomials as basis functions. Since there are no boundary conditions for density (particle volume fraction), the staggered grid method (Canuto *et al.* 1988; Alam & Nott 1998) has been employed: the continuity equation is collocated at Gauss points and the other three equations (x and y momentum equations and the granular energy equation) at Gauss–Lobatto points; the spectral interpolation matrices are used to transform variables from Gauss to Gauss–Lobatto grids.

With the above spectral discretization scheme, the linear eigenvalue problem (3.22) is transformed into a matrix eigenvalue problem,

$$
\boldsymbol{A} X^{[1;1]} = c^{(0)} \boldsymbol{B} X^{[1;1]},
\tag{5.1}
$$

where $\boldsymbol{A}$ and $\boldsymbol{B}$ are square matrices of size $(4M + 3)$, with M being the degree of Chebyshev polynomials; there are $(4M + 3)$ number of eigenvalues $c^{(0)}$, and each mode corresponds to an eigenvector $X^{[1;1]}$. The above problem (5.1) has been solved using the QZ-algorithm, which yields all eigenvalues at a time. For the fundamental mode, we have used a normalization such that

$$
\max_y |T^{[1;1]}(y)| = T^0,
\tag{5.2}
$$

where T^0 is the base state temperature as defined in (2.17). Such a normalization is directly tied to the fact that the nonlinear perturbation amplitude A is measured in terms of temperature perturbation which can be linked to pressure perturbation. For the nonlinear stability, each of the inhomogeneous system of equations (3.24), (3.23), (3.20) and (3.29) has been solved using the singular value decomposition (SVD) method. To evaluate the integrals in the solvability condition (3.25), the Gauss–Chebyshev quadrature formula (Shukla & Alam 2011) has been used. We have used Matlab software for all these computations.

The details on the accuracy of our numerical method over other equivalent numerical methods for the special case of shear-banding instabilities ($k_x = 0$) can be found in Shukla & Alam (2011). For the present case with $k_x \neq 0$, it has been verified that about 30 collocation points are enough to obtain converged eigenvalues (with an error less than 1 %). For an accurate computation of the first Landau coefficient, we needed $M \sim 50$ if the Couette gap is $H \leqslant 100$; for larger Couette gaps $H > 100$, we have used $M = 100$ or more collocation points.

There are four control parameters to describe the granular plane Couette flow: (i) the mean density or the volume fraction of particles ϕ^0, (ii) the Couette gap $H = \overline{h}/\overline{d}$ (i.e. the gap between two walls in terms of particle diameter) and (iii) the restitution coefficient e. For stability, we have an additional parameter: (iv) the dimensionless streamwise wavenumber

$$k_x = \frac{2\pi}{\lambda_x}, \quad \text{with} \quad \lambda_x = \frac{\overline{\lambda}_x}{\overline{h}} \tag{5.3}$$

being the dimensionless wavelength of perturbation. Note that λ_x sets the streamwise length of the Couette cell in the sense that for any perturbation with wavelength λ_x to grow, the channel length must be large enough (i.e. $\overline{l}_x/\overline{h} > \lambda_x$, where $\overline{l}_x$ is the length of the Couette cell and $\overline{\overline{h}}$ is its height; see figure 1) to accommodate it.

6. Results and discussion: Hopf and pitchfork bifurcations, and resonances

It is known (Alam & Nott 1998) that the plane Couette flow is unstable to shear-banding ($k_x = 0$), stationary and travelling instabilities with $k_x \neq 0$ for a range of particle volume fractions (ϕ^0) and Couette gaps (H) at any restitution coefficient $e < 1$. Let us focus on the specific case of $H = 100$, $\phi^0 = 0.2$ and $e = 0.8$, for which all the above instabilities coexist. For these parameters the variations of the growth rate of the least-stable mode, $a_l^{(0)}$, and its phase velocity c_{ph} (see (4.3)) are shown in figure 3 by the solid and dot-dashed lines, respectively. We define the least-stable mode (or the leading eigenvalue) as the eigenvalue having the maximum real part for a given wavenumber k_x:

$$a_l^{(0)} = \max a^{(0)}, \tag{6.1}$$

out of all $(4M+3)$ eigenvalues of (5.1), where $(M+1)$ is the number of Gauss–Lobatto collocation points (momentum and energy equations) and M is the number of Gauss collocation points (continuity equation). While the solid and dot-dashed lines in figure 3 correspond to results with $M = 50$, the circles and crosses refer to results with $M = 75$ and 100 collocation points, respectively. This validates the convergence of our numerical results with $M = 50$ collocation points; for most computations, about $M = 75$ collocation points have been used.

In figure 3, the phase velocity corresponding to the first peak of the growth rate curve is zero, which represents a stationary instability. Similarly, the phase velocity for the second peak is non-zero and thus the flow is unstable due to travelling waves
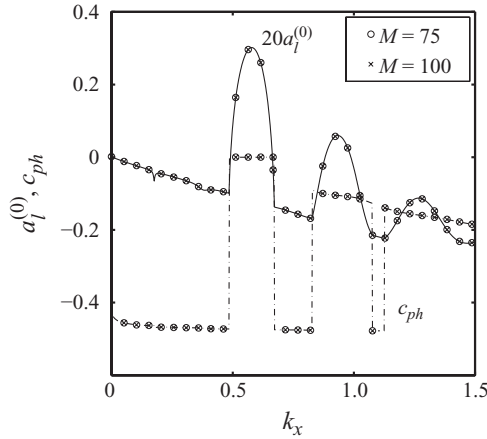
FIGURE 3. Variations of the growth rate (solid line) and the phase velocity (dot-dashed line) of the least-stable mode for $\phi^0 = 0.2$, $H = 100$ and $e = 0.8$, with $M = 50$ collocation points. The circles and crosses refer to results with $M = 75$ and 100, respectively.
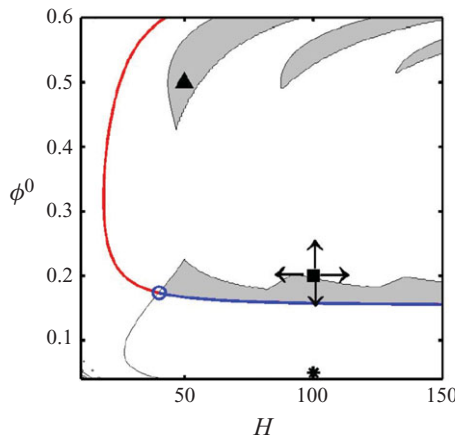

FIGURE 4. (Colour online) Phase diagram for the nonlinear instability of shear-banding modes ($k_x = 0$); the restitution coefficient is $e = 0.8$. The thick red/blue contour represents 'critical line' at which the linear growth rate is zero, i.e. $a^{(0)} = 0$, and the thin black contours represent zeros of the first Landau coefficient $a^{(2)} = 0$; the grey-shaded region corresponds to $a^{(0)} > 0$ and $a^{(2)} > 0$. The square, star and triangle symbols refer to points at which most of the nonlinear results with $k_x \neq 0$ will be presented. The blue circle is the degenerate point.

there. For parameter values of figure 3, the flow is also unstable to the shear-banding mode ($k_x = 0$); moreover, there are other stationary and travelling wave instabilities at very long wavelengths ($k_x = 2\pi/\lambda_x \sim 0$) as we discuss next in §6.1.

6.1. *Nonlinear shear-banding ($k_x = 0$) and long-wave ($k_x \sim 0$) instabilities*

Before presenting results for $k_x \neq 0$, let us briefly recall nonlinear results for shear-banding modes ($k_x = 0$) since they eventually give birth to long-wave instabilities. Figure 4 presents a phase diagram in the (ϕ^0, H)-plane for a restitution coefficient of $e = 0.8$, delineating the regimes of supercritical and subcritical flows. The thick contour in figure 4 corresponds to the zero growth rate [$a^{(0)} = 0$], representing the critical line, and the thin contours represent the zeros of the first Landau coefficient [$a^{(2)} = 0$]. In

figure 4, $a^{(2)}$ has been calculated that corresponds to the shear-banding mode ($k_x = 0$) having the maximum growth rate over all possible gradient wavenumbers ($k_\beta = \beta\pi$, with $\beta = 1, 2, 3, \ldots$, being the mode number; the value of the mode number β corresponds to the number of zero crossings, along y, of the density eigenfunction; see Shukla & Alam 2011). The grey-shaded regions in figure 4 correspond to $a^{(0)} > 0$ and $a^{(2)} > 0$, in which there are 'growing' nonlinear solutions at cubic order, and this calls for higher-order Landau coefficients (not calculated here) to locate the related stable solutions, if any. The point at which the growth rate and the first Landau coefficient are simultaneously zero [$a^{(0)} = 0 = a^{(2)}$] is known as the 'degenerate' point, shown by the blue circle in figure 4 at $\phi_s \approx 0.1735$. The red upper branch of the critical line above the degenerate point in figure 4 is supercritically stable, and the blue lower branch is subcritically unstable. The nonlinear equilibrium solutions of shear-banding-type appear via a supercritical bifurcation for $\phi^0 > \phi_s$ and via a subcritical bifurcation for $\phi^0 < \phi_s$ below it (Shukla & Alam 2011).

In addition to the shear-banding instability, there are long-wave ($k_x \sim 0$) stationary and travelling instabilities whose origin can be tied to the shear-banding modes (Alam & Nott 1998) – these long-wave modes might be unstable/stable and might be responsible for supercritical and subcritical nonlinear solutions as we discuss next in §6.1.1.

6.1.1. *Long-wave modes* ($k_x \sim 0$)

The variations of the growth rate of the least-stable mode $a_l^{(0)}$ and its phase velocity (inset plot) with wavenumber k_x are shown in figure 5(a). The parameter values are $\phi^0 = 0.2$, $H = 100$ and $e = 0.8$, which correspond to the 'square' symbol in figure 4. The shear-banding mode corresponds to $k_x = 0$, which is unstable [$a^{(0)} > 0$ and $a^{(2)} < 0$]. It is seen that the flow remains unstable to stationary disturbances with long wavelengths (i.e. $k_x = 2\pi/\lambda_x \sim 0$) up to a wavenumber of $k_x \sim 2.1 \times 10^{-5}$, and thereafter to travelling waves (see the inset for phase velocity in figure 5a). In fact, two stationary modes merge together at $k_x \sim 2.1 \times 10^{-5}$ to yield a pair of forward- and backward-propagating travelling waves which remain unstable for a range of k_x. It can be verified (Alam & Nott 1998) that the linear eigenvalue problem (3.22) is invariant under the transformation

$$(x, y, t) \rightarrow (-x, -y, t), \quad [\phi', u', v', T'] \rightarrow [\phi', -u', -v', T'], \tag{6.2}$$

$$\Rightarrow [\hat{\phi}, \hat{u}, \hat{v}, \hat{T}](y)\exp\left(c^{(0)}t + \mathrm{i}k_x x\right) \rightarrow [\hat{\phi}, -\hat{u}, -\hat{v}, \hat{T}](-y)\exp\left(c^{(0)}t - \mathrm{i}k_x x\right). \tag{6.3}$$

This implies that a forward-propagating wave ($c_{ph} \equiv -b^{(0)}/k_x > 0$: see (4.3)) always coexists with a backward-propagating wave ($c_{ph} < 0$) in the plane Couette flow.

In figure 5(b), we show the variations of the real, $a^{(2)}$, and the imaginary, $b^{(2)}$, parts of the first Landau coefficient for small k_x. The sharp jump in each curve of figure 5(b) at $k_x \sim 2.1 \times 10^{-5}$ indicates a mode-switching between stationary and travelling waves. The variations of the equilibrium amplitude A_e and the equilibrium phase velocity c_{ph}^e are shown in figures 5(c) and 5(d), respectively. Note that the bifurcation-type changes from pitchfork (static/stationary) to Hopf (dynamic/oscillatory) at $k_x \sim 2.1 \times 10^{-5}$ due to the above-mentioned switchover from stationary to travelling waves. For the range of k_x in figure 5, $a^{(0)} > 0$ and $a^{(2)} < 0$ for both stationary and travelling waves, and hence the bifurcations are supercritical in nature for both cases.

Fixing the Couette gap at $H = 100$, we now move to the dilute regime of $\phi^0 = 0.05$ (the 'star' symbol in figure 4), where the plane Couette flow is subcritically unstable to shear-banding instability. Figure 6(a) shows the variation of the growth rate of the least-stable mode for small k_x, with the corresponding variation of the phase velocity
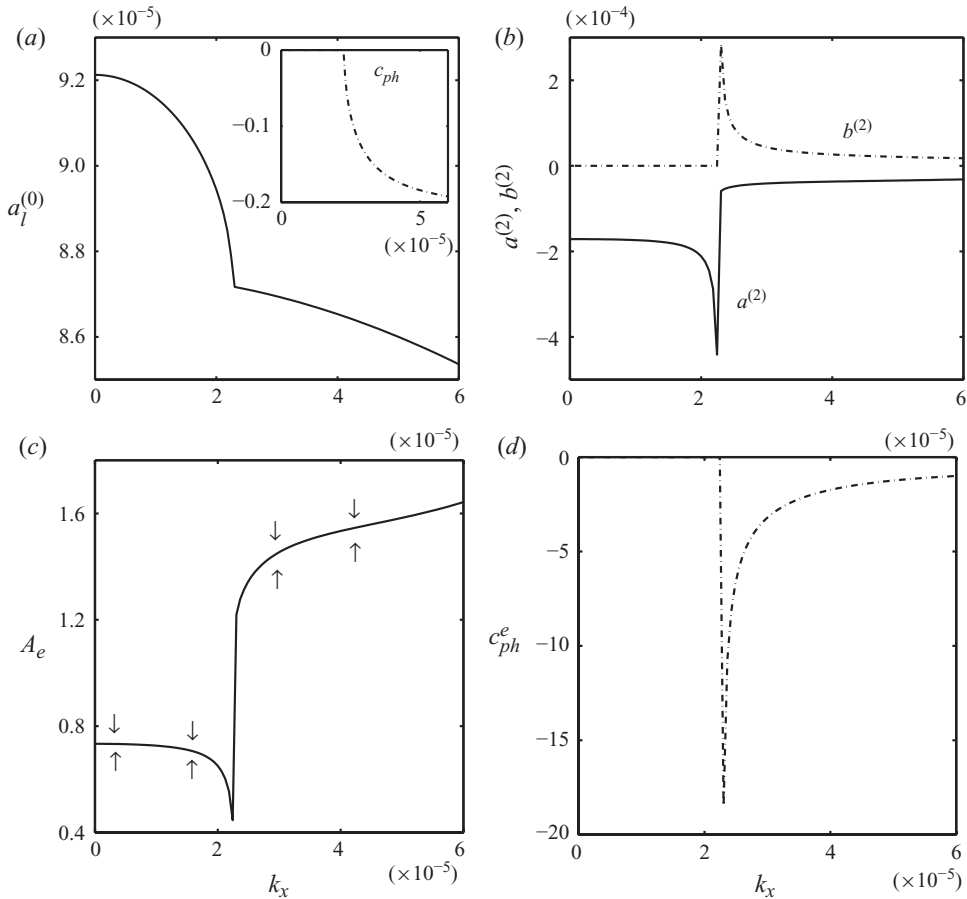
FIGURE 5. Long wavelength variations at $\phi^0 = 0.2$, $H = 100$ and $e = 0.8$: (a) linear growth rate and phase velocity (inset) of the least-stable mode; (b) $a^{(2)}$ (solid line) and $b^{(2)}$ (dot-dashed line) with k_x; (c) equilibrium amplitude with k_x; (d) equilibrium phase velocity.

being displayed as an inset. The growth rates remain negative for both stationary and travelling waves, and hence the flow is linearly stable at long waves $k_x \sim 0$ (and we have verified that the flow is stable at any k_x for this parameter set). However, the variations of the first Landau coefficient in figure 6(b) clearly show that $a^{(2)} > 0$ for a range of $k_x \sim 0$ that represents only stationary waves. Therefore, the finite-amplitude nonlinear solutions exist for stationary instabilities at long waves, as shown in the inset of figure 6(b). Note that the corresponding nonlinear solutions are unstable since the underlying bifurcation is subcritical [$a^{(0)} < 0$ and $a^{(2)} > 0$]; therefore A_e in figure 6(b) provides a threshold for nonlinear stability in the sense that for any finite-amplitude perturbation with $A < A_e$ the uniform shear flow will be recovered; however, with $A > A_e$ the flow will reach a new stable equilibrium solution. To locate this stable finite-amplitude solution we need to calculate the second Landau coefficient, which has not been pursued in this paper.

Lastly, we consider the parameter values corresponding to the 'triangle' symbol in figure 4 ($\phi^0 = 0.5$ and $H = 50$) at which the nonlinear shear-banding solutions ($k_x = 0$) are growing since $a^{(0)} > 0$ and $a^{(2)} > 0$. The long-wave variations of $a^{(0)}$ and c_{ph} are shown in the main panel and the inset of figure 7(a), respectively. It is seen
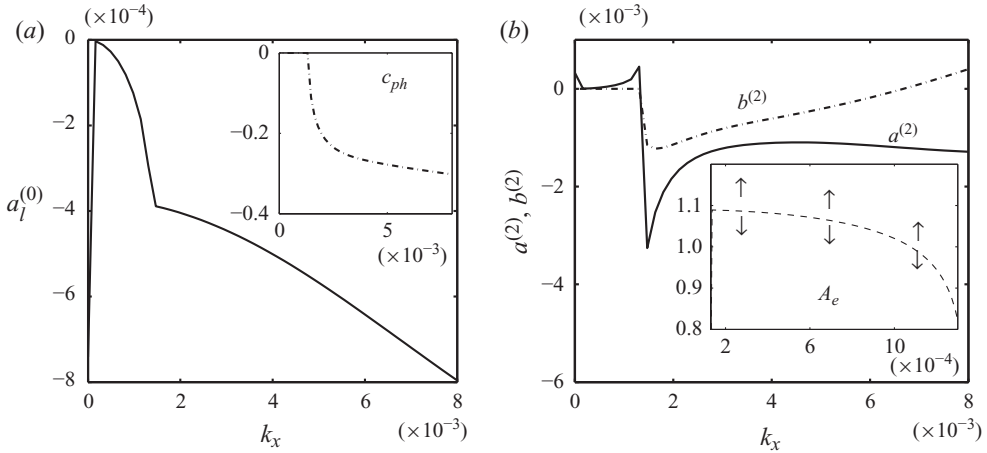
FIGURE 6. Long wavelength variations in the dilute limit ($\phi^0 = 0.05$): (a) $a_l^{(0)}$ (main panel) and c_{ph} (inset); (b) $a^{(2)}$ and $b^{(2)}$ (main panel), and equilibrium amplitude A_e (inset). Other parameters are the same as in figure 5.
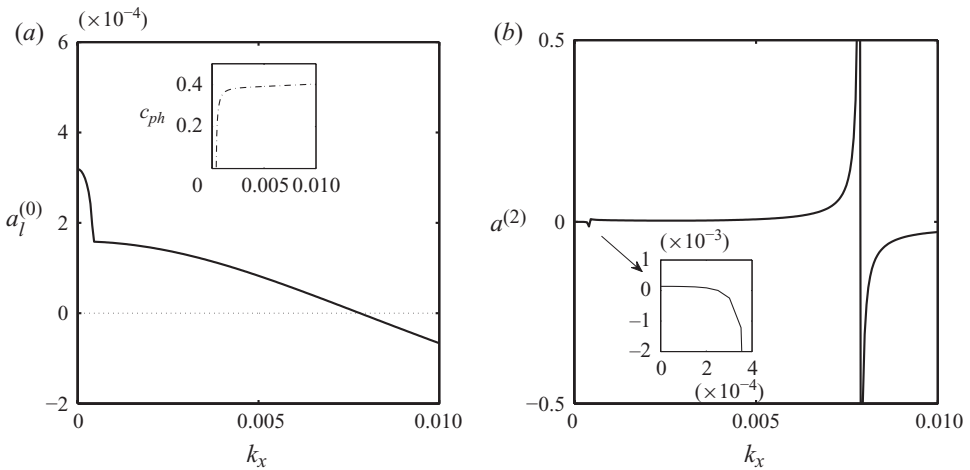
FIGURE 7. Long wavelength variations for dense flows at $\phi^0 = 0.5$ (corresponding to the triangle symbol in figure 4 at $H = 50$): (a) $a_l^{(0)}$ (main panel) and c_{ph} (inset); (b) $a^{(2)}$.

that the flow is unstable to stationary and travelling waves up to a wavenumber $k_x \sim 0.008$, and stable thereafter. The corresponding variation of $a^{(2)}$ with k_x is shown in figure 7(b). Note that $a^{(2)}$ diverges and changes its sign at $k_x \sim 0.008$; the divergence of $a^{(2)}$ is in fact tied to the onset of nonlinear resonance, which will be discussed in §6.3. Within the wavenumber band $k_x \sim (0, 0.008)$, $a_l^{(0)} > 0$ but $a^{(2)}$ also remains positive except over an extremely small range of k_x (see the inset of figure 7b) just below the mode-switching point, located at $k_x \approx 3.8 \times 10^{-4}$, at which two unstable stationary modes merge to yield a pair of unstable travelling waves. Therefore, at $\phi^0 = 0.5$ and $H = 50$, the flow remains nonlinearly stable except near $k_x \approx 3.8 \times 10^{-4}$.

Figures 8 and 9 show a comparison between nonlinear and linear disturbance patterns for long-wave stationary and travelling instabilities, respectively, of figure 5 – the wavenumbers are $k_x = 10^{-5}$ and 4×10^{-5}, respectively. The nonlinear disturbance
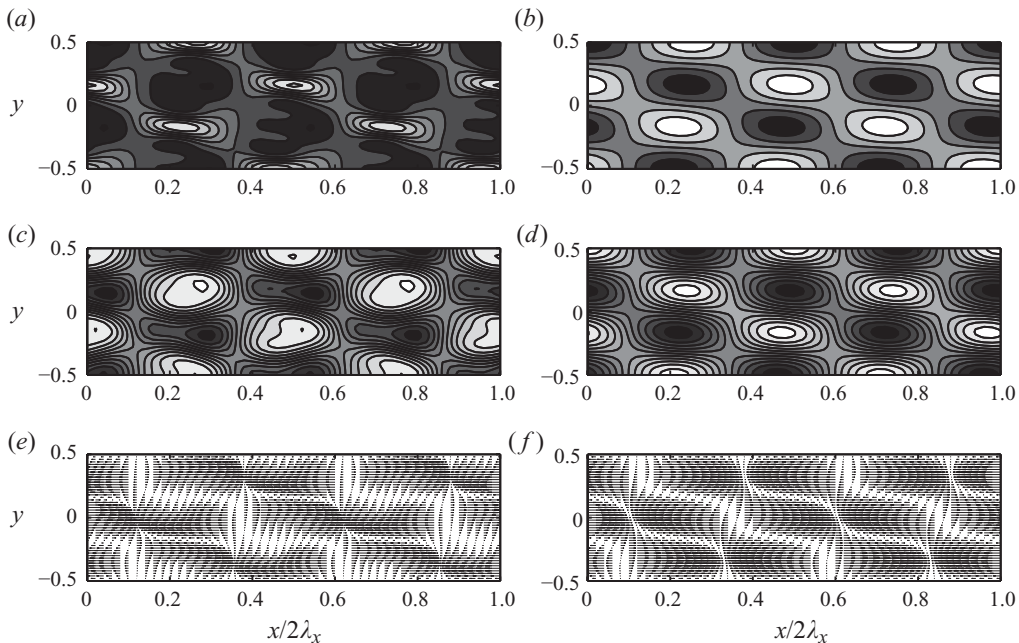
FIGURE 8. Long-wave patterns of (a, b) density, (c, d) granular temperature and (e, f) velocity field with $k_x = 10^{-5}$. Parameter values are the same as in figure 5.

pattern is calculated using (4.8), which is correct up to cubic order $O(A^3)$, and the linear disturbance field is calculated by setting $O(A^2)$- and $O(A^3)$-terms to zeros in (4.8). Figures 8(a, c, e), 9(a, c, e) and 8(b, d, f), 9(b, d, f) correspond to nonlinear and linear patterns, respectively; while figures 8(a–d) and 9(a–d) show the grey-scale maps of the perturbation density ϕ' and granular temperature T', those in figures 8(e, f) and 9(e, f) display the vector plots of the perturbation velocity field (u', v'). On the grey scale, the black and white represent minimum and maximum values, respectively. The linear eigenfunction of the stationary instability in figure 8(b, d, f) contains two rows of particle clusters (density maxima) across the gradient direction y (see also the temperature eigenfunction in figure 8d): this is because the parental origin of this long-wave stationary instability at $H = 100$ (refer to the 'square' symbol in figure 4) is the 'mode 2' shear-banding instability whose density eigenfunction has two zero-crossings across y (Shukla & Alam 2011). The corresponding nonlinear equilibrium solution in figure 8(a, c, e) is a modulated version of the linear eigenfunction in figure 8(b, d, f). Note that the temperature is maximum at the location of minimum density, and the velocity field is seen to be changing its direction at the location of density maxima.

The long-wave travelling solution displayed in figure 9 corresponds to a backward-propagating mode. For this instability, the nonlinear fields in figure 9(a, c, e) appear to be much more distorted from their linear counterparts in figure 9(b, d, f). Other features look similar to those for the stationary mode in figure 8.

6.2. *Nonlinear results on stationary and travelling instabilities:* $k_x \sim O(1)$

We now focus on the instabilities due to the first peak of figure 3: for the wavenumber band $k_x \sim (0.5, 0.65)$ in figure 3, the phase velocity is zero and the growth rate is positive, and hence the flow is linearly unstable to stationary waves. The corresponding
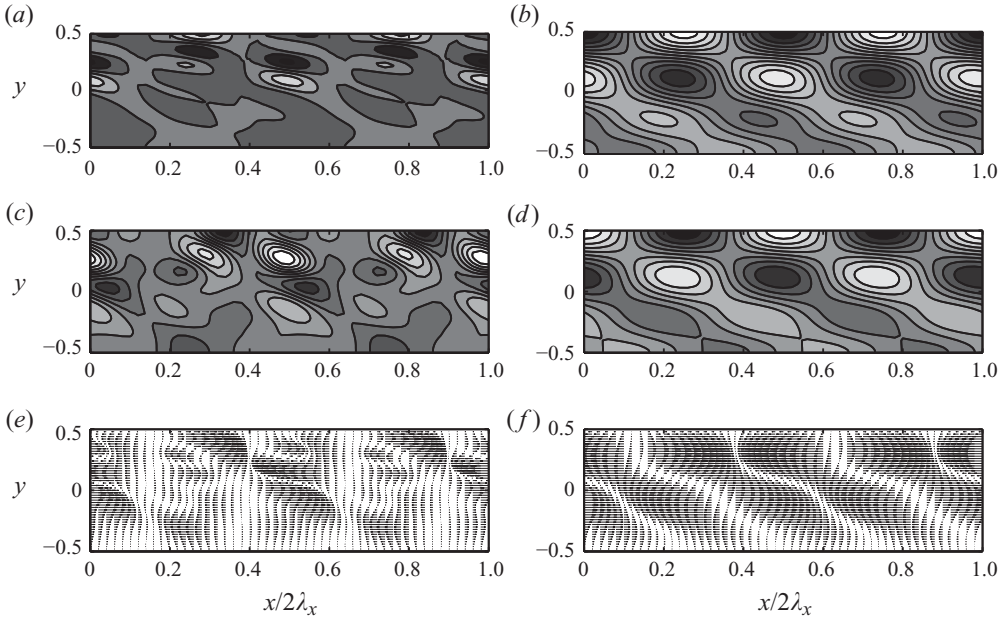
FIGURE 9. Same as figure 8, but for long-wave travelling instability at $t = 0$ with $k_x = 4 \times 10^{-5}$.

variation of the real part of the first Landau coefficient, $a^{(2)}$, with k_x is shown in figure 10(a); the imaginary part, $b^{(2)}$, is not shown since it remains zero for stationary waves. It is clear that $a^{(2)}$ is negative for $k_x \sim (0.5, 0.65)$ but $a^{(0)}$ is positive there, and hence there are stable nonlinear solutions, with the equilibrium amplitudes as displayed in figure 10(b). Because of the stationary nature of the underlying instability, we have supercritical pitchfork/static bifurcations within the wavenumber band $k_x \sim (0.5, 0.65)$ in figure 3.

Note that varying the streamwise wavenumber k_x is equivalent to varying the channel length since the 'minimum' length of the channel (see figure 1) is given by

$$l_x^{min} = \frac{\overline{\lambda_x}}{\overline{d}} = \frac{2\pi H}{k_x} \leqslant \frac{\overline{l_x}}{\overline{d}}, \tag{6.4}$$

and therefore the range of channel lengths in figure 10 corresponds to $l_x \in (12.56 - 9.75)H$ at a Couette gap of $H \equiv l_y/d = 100$. This has important implications for molecular dynamics or hydrodynamic simulations of the granular Couette flow: the nonlinear instabilities such as those in figure 10(b) can be realized if the simulations are carried out in a rectangular box such that its aspect ratio is $l_x/l_y \geqslant 9.75$ with $H = 100$. This should be kept in mind while making any comparison between the present theoretical results and simulations, as done briefly in §6.6.

A comparison between the nonlinear and linear patterns of density, granular temperature and velocity is shown respectively in figures 11(a, c, e) and 11(b, d, f). On the grey scale in figure 11(a, d), the white represents maximum and the black represents minimum; the vector plot of the velocity field (u, v) is displayed in figure 11(e, f). The nonlinear density and temperature fields are seen to be highly distorted from their linear counterparts: the location of the density maxima for the nonlinear case (compare figures 11a and 11b) shifts away from the walls into the bulk. With nonlinear corrections, the pockets of dilute and dense zones in figures 11(a)
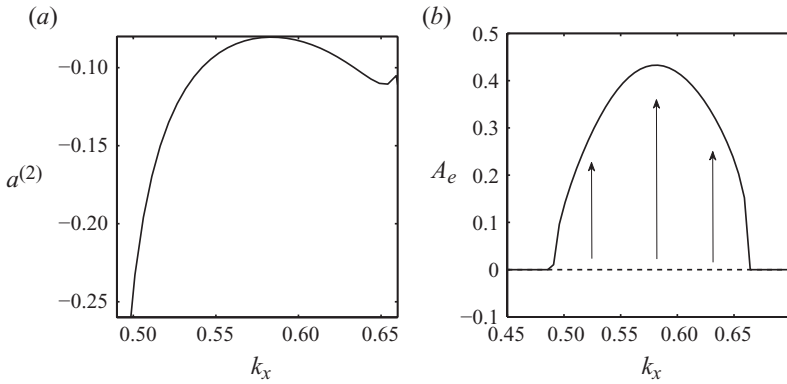
FIGURE 10. Variations of (*a*) the first Landau coefficient $a^{(2)}$ and (*b*) the equilibrium amplitude A_e with wavenumber k_x. Parameter values are as in figure 3.
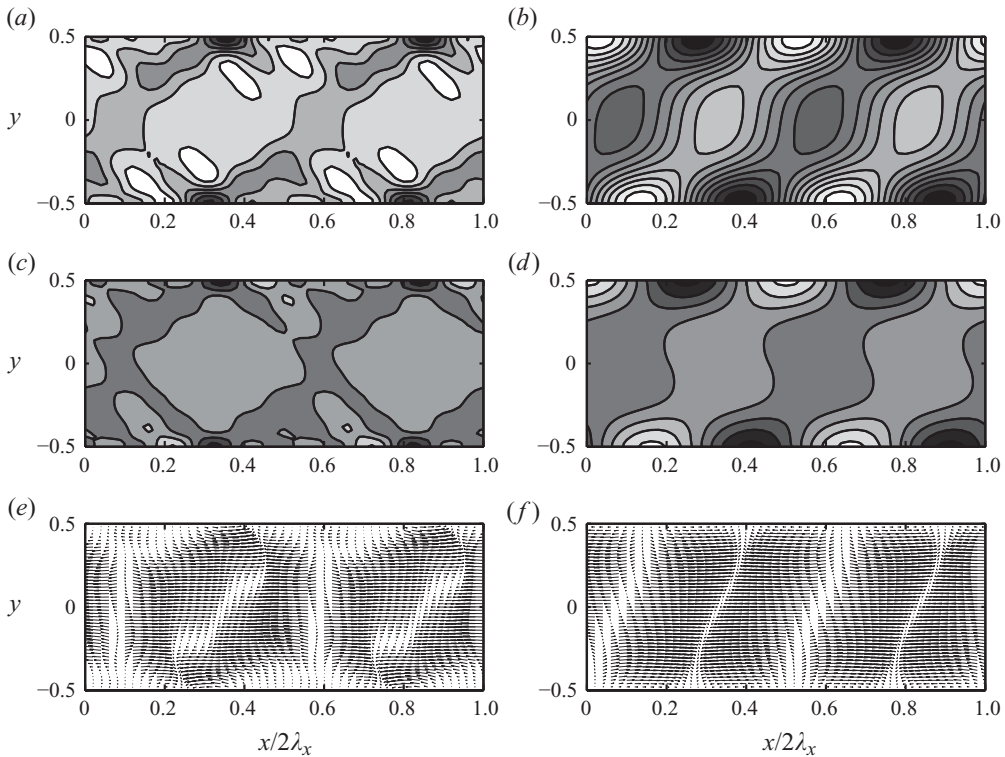

FIGURE 11. Patterns of (*a*, *b*) perturbation density $\phi'(x, y)$, (*c*, *d*) granular temperature $T'(x, y)$ and (*e*, *f*) velocity (u', v'), for the dominant stationary mode in figure 10 at $k_x = 0.5858$. Panels (*a*, *c*, *e*) represent nonlinear patterns, while (*b*, *d*, *f*) represent linear eigenfunction. Other parameter values are $H = 100$, $e = 0.8$ and $\phi^0 = 0.2$, as in figure 3.

and 11(*c*) are seen to be tenuously distributed in the (x, y)-plane. To ascertain the true aspect ratio of the plots in figure 11, we must stretch the x-axis by a factor of about $2\pi/k_x \approx 10.72$, since $k_x = 0.5858$ for these plots. A comparison of the linear eigenfunctions in figure 11(*b*, *d*, *f*) with those in figure 8(*b*, *d*, *f*) suggests
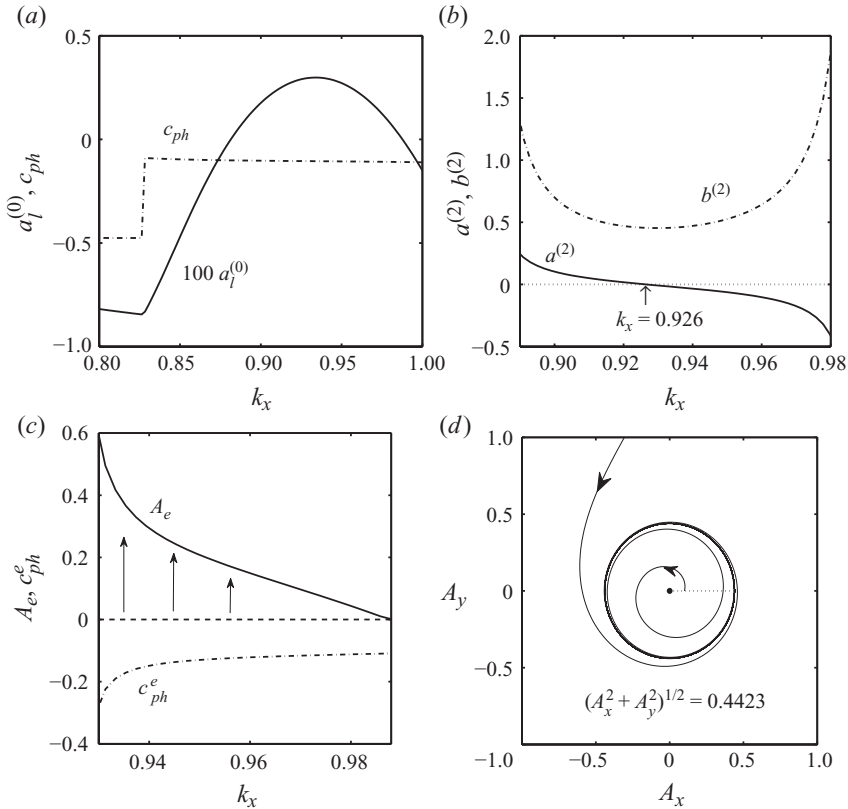
FIGURE 12. Variations with k_x of (a) the growth rate, $100a_l^{(0)}$ (solid line), and the phase velocity, c_{ph} (dot-dashed line), of the least-stable travelling mode; (b) the first Landau coefficient: real part (solid line), imaginary part (dot-dashed line); and (c) the equilibrium amplitude A_e (solid line) and the equilibrium phase velocity c_{ph}^e (dot-dashed line); parameter values are as in figure 3. (d) Stable limit cycle and two spiralling orbits in the (A_x, A_y)-plane at $k_x = 0.93$.

that the structural features of the 'dominant' stationary instability (at $k_x \sim O(1)$) are significantly different from those for 'long waves' (at $k_x \sim 0$) stationary instability.

For the wavenumber band around the second peak in figure 3, we show the variations of growth rate (solid line) and the phase velocity (dot-dashed line) in figure 12(a): clearly, the flow is unstable to travelling waves. (It may be noted that the growth rates of these travelling waves at $k_x = O(1)$ are an order of magnitude larger than those at long waves $k_x \sim 0$: see figure 5.) The corresponding variations of the real (solid line) and the imaginary (dot-dashed line) parts of the first Landau coefficient are shown in figure 12(b). The real part of the first Landau coefficient ($a^{(2)}$) changes its sign from positive to negative at $k_x \approx 0.926$, shown by an arrow in figure 12(b). Since the underlying instability is oscillatory, we have supercritical Hopf/oscillatory bifurcations within the wavenumber band $k_x \in (0.926, 0.99)$. The corresponding equilibrium amplitude (solid line) and the equilibrium phase velocity (dot-dashed line) are shown in figure 12(c). Note that even though the flow is unstable to travelling waves (i.e. $a^{(0)} > 0$: see figure 12a) over $k_x \in (0.88, 0.926)$, the nonlinear equilibrium solutions do not exist over $k_x \in (0.88, 0.926)$ since $a^{(2)} > 0$ there (see figure 12b).
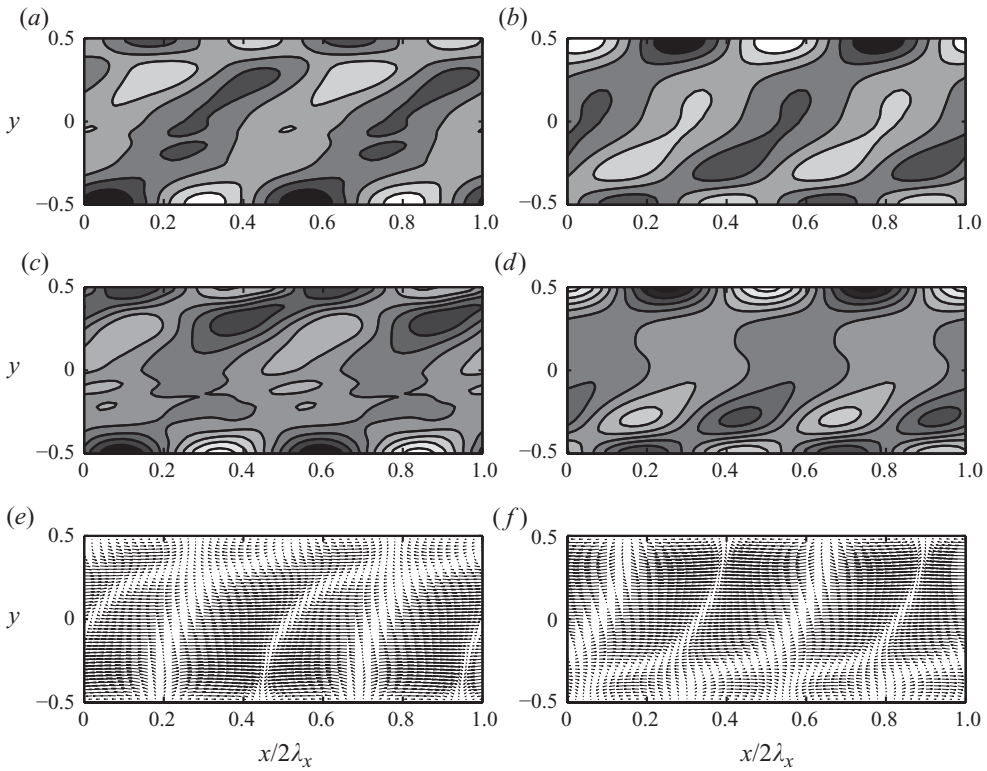
FIGURE 13. Same as figure 11, but for the dominant travelling wave at $t = 0$ with $k_x = 0.93$.

The cubic Landau–Stuart equations (4.4)–(4.5) have exact analytical solutions:

$$A^2(t) = \frac{a^{(0)} A_0^2}{\left[a^{(0)} + a^{(2)} A_0^2\right] \exp(-2a^{(0)}t) - a^{(2)} A_0^2}, \tag{6.5}$$

$$\theta(t) = \theta_0 + b^{(0)}t - \frac{b^{(2)} a^{(0)}}{a^{(2)}} \ln \left[\frac{a^{(0)} + a^{(2)} A_0^2 (1 - \exp(-2a^{(0)}t))}{a^{(0)}} \right], \tag{6.6}$$

with $a^{(0)} \neq 0$, where $A_0 \equiv A(t = 0)$ and $\theta_0 \equiv \theta(t = 0)$ are initial conditions. At $k_x = 0.93$ and other parameters of figure 12(c), the coefficients of (4.4)–(4.5) are $a^{(0)} \approx 2.9711 \times 10^{-3}$, $b^{(0)} \approx 9.7524 \times 10^{-2}$, $a^{(2)} \approx -1.5185 \times 10^{-2}$ and $b^{(2)} \approx 7.7618 \times 10^{-1}$. For these parameters, the equilibrium amplitude is $A_e = \sqrt{-a^{(0)}/a^{(2)}} \approx 0.4423$. We have evaluated the exact solution trajectories (6.5)–(6.6) for two initial conditions: one with $A_0 > A_e$ and other with $A_0 < A_e$, with $\theta_0 = 0$. These solutions are indicated by solid lines in figure 12(d) in the (A_x, A_y)-plane, where $A_x = A \cos\theta$ and $A_y = A \sin\theta$. Both spiralling orbits asymptotically approach a limiting circle of radius $A = A_e$ as $t \to \infty$ – this is the limit cycle, which is stable for the present case.

For the dominant travelling wave instability of figure 12 that occurs at $k_x \approx 0.93$, the nonlinear and linear perturbation fields of density, granular temperature and velocity are compared in figure 13: this is a backward-propagating mode. To visualize the true aspect ratio of these plots, we need to stretch the x-axis by a factor of about $2\pi/k_x \approx 6.75$, and therefore the density bands, for example in figure 13(a), are much more elongated than what is seen here. In contrast to the case of stationary instability in figure 11, the nonlinear corrections induce a significant change in the velocity field
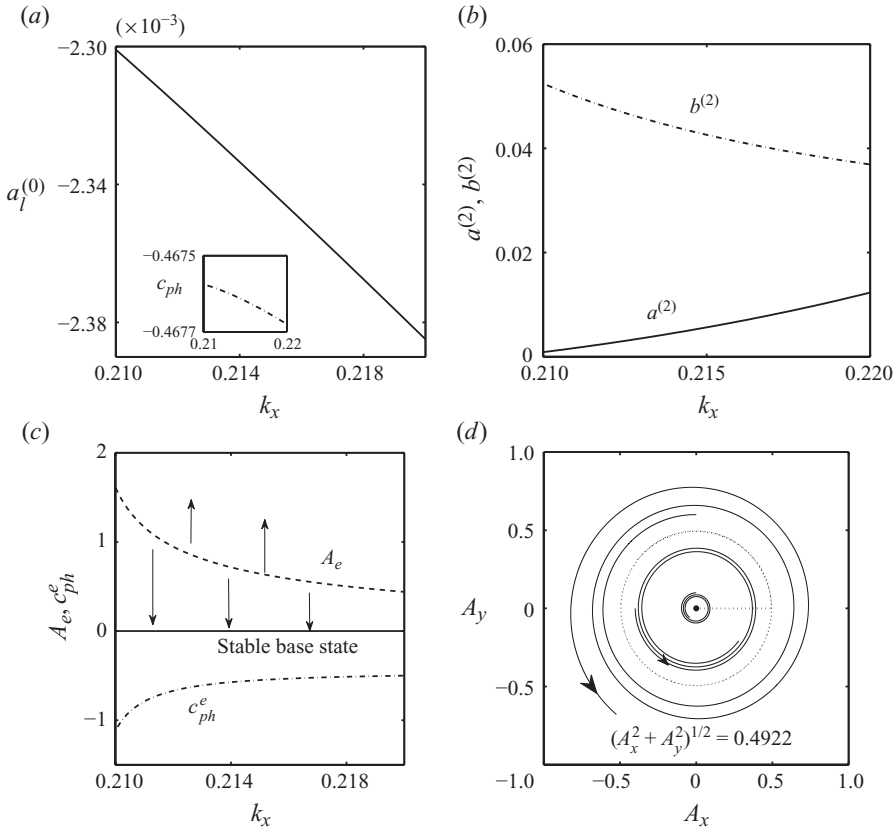
FIGURE 14. Variations of (a) $a_l^{(0)}$ (main panel) and c_{ph} (inset), (b) $a^{(2)}$ (solid line) and $b^{(2)}$ (dot-dashed line), and (c) A_e (dashed line) and c_{ph}^e (dot-dashed line) with k_x; other parameters are the same as in figure 3. (d) Unstable limit cycle and two spiralling orbits at $k_x = 0.215$.

(compare figures 13e and 13f); the nonlinear density and temperature fields have some resemblance to their linear counterparts, even though they are also distorted like the velocity field. In particular, the nonlinear velocity field shows vortical-type motions (not shown for brevity) if we analyse the total velocity $(u, v) = (u^0 + u', v + v')$.

The evidence of subcritical instability at moderate values of k_x is shown in figure 14 for a range of wavenumbers $k_x \in (0.21, 0.22)$; other parameters are as in figure 3. While the variations of the growth rate of the least-stable mode and the phase velocity (inset) are shown in figure 14(a), the first Landau coefficient is shown in figure 14(b). These are 'stable' $[a^{(0)} < 0]$ travelling waves as seen in figure 14(a). Since $a^{(2)}$ and $a^{(0)}$ are of opposite signs over $k_x \in (0.21, 0.22)$, this leads to 'subcritical' Hopf bifurcations, with oscillatory nonlinear solutions. The corresponding variations of the equilibrium amplitude A_e and the equilibrium phase velocity c_{ph}^e are shown in figure 14(c) by dashed and dot-dashed lines, respectively. As discussed in §4.2, the equilibrium amplitude in figure 14(c) provides a measure for the 'threshold' amplitude for nonlinear stability since we have calculated only the first Landau coefficient. Figure 14(d) shows the limit cycle (dashed circle) at $k_x = 0.215$ with other parameters as in figure 14(c). For these parameters, the coefficients of the Landau–Stuart equations (4.4)–(4.5) are $a^{(0)} \approx -2.3418 \times 10^{-3}$, $b^{(0)} \approx 1.0053 \times 10^{-1}$, $a^{(2)} \approx 9.6679 \times 10^{-3}$ and $b^{(2)} \approx 7.2967 \times 10^{-2}$; the corresponding equilibrium amplitude is $A_e = \sqrt{-a^{(0)}/a^{(2)}} \approx 0.4922$. The solution
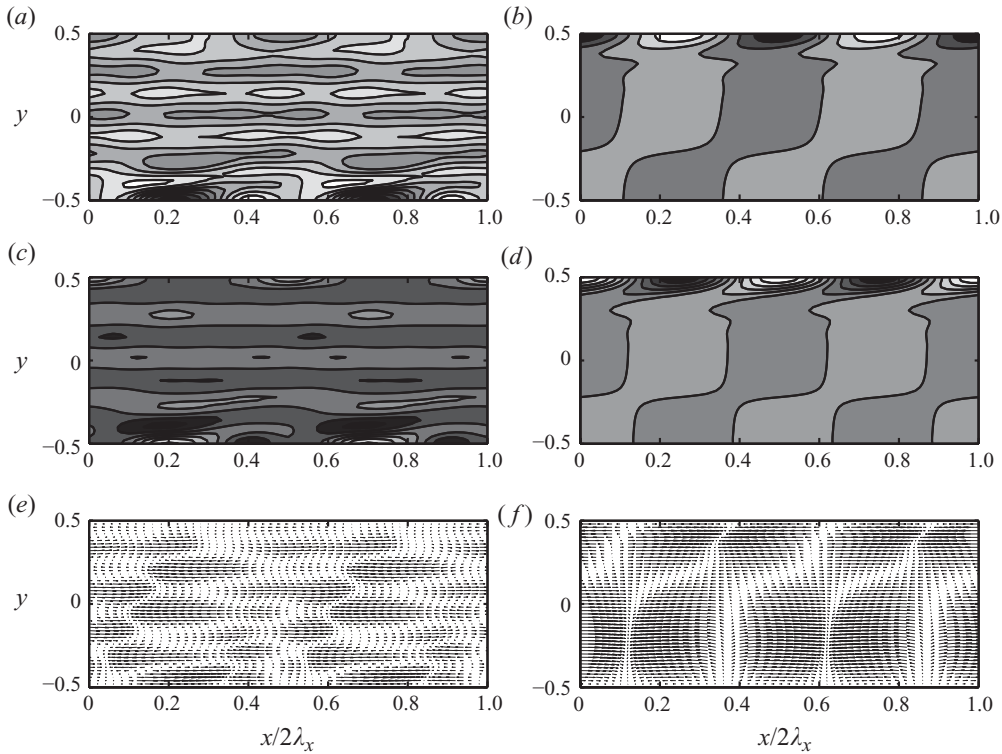
FIGURE 15. Same as figure 13, but for the subcritical travelling wave at $t = 0$ with $k_x = 0.215$ with parameter values as in figure 14(d).

trajectories (6.5)–(6.6) for two initial conditions (one inside the limit cycle and the other outside) are plotted by solid lines in figure 14(d): both orbits spiral away from the limit cycle (dashed circle) as $t \to \infty$, confirming that this represents an 'unstable' limit cycle.

With parameter values as in figure 14(d), the nonlinear and linear patterns are compared in figure 15(a–f). Recall that this is an 'unstable' subcritical travelling wave. Unlike the supercritical solutions in figure 13, the nonlinear subcritical patterns in figure 15(a, c, e) have little resemblance to their linear eigenfunctions in figure 15(b, d, f). The structural features of all perturbation fields in figure 15(a, c, e) appear to be elongated and aligned along the streamwise direction, and the pockets of dilute and dense regions are tenuously distributed in the (x, y)-plane.

6.3. *Evidence of mean-flow resonance and 1 : 2 resonance*

We first consider the mean-flow resonance condition (3.32) which represents a resonant interaction between a linear mode at some value of k_x and a shear-banding mode (i.e. a disturbance at zero wavenumber $k_x = 0$). Focusing on the wavenumber band $k_x = (0.26, 0.38)$ with other parameters as in figure 3, we have plotted the variations of the least-stable growth rate and its phase velocity in figure 16(a) and that of $a^{(2)}$ (solid line) and $b^{(2)}$ (dot-dashed line) with wavenumber in figure 16(b). Note that in figure 16(b), $a^{(2)}$ has a kink near $k_x \sim 0.365$, which is a consequence of the mean-flow resonance condition being satisfied, as we show below.

Recall from (3.32) that the condition for the mean-flow resonance is $2a_{j1}^{(0)}(k_x) = a_{j2}^{(0)}(k_x = 0)$ with $b_{j2}^{(0)}(k_x = 0) = 0$ for any two modes $j1$ and $j2$. In figure 16(c),
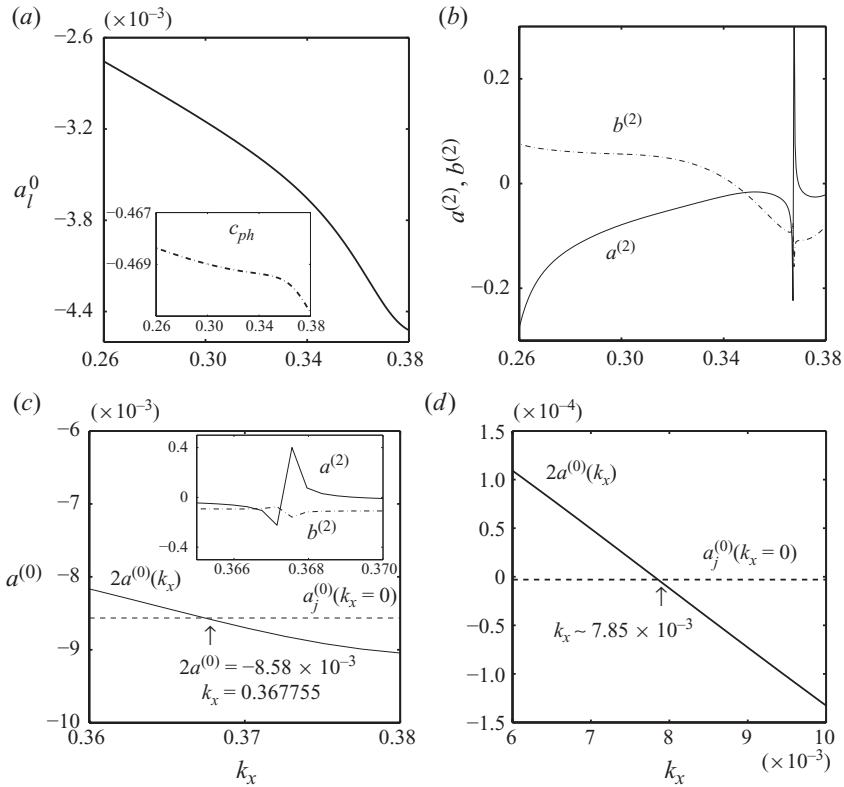
FIGURE 16. Variations of (a) $a_l^{(0)}$ (main panel) and c_{ph} (inset plot) and (b) $a^{(2)}$ (solid line) and $b^{(2)}$ (dot-dashed line). Evidence of the mean-flow resonance at (c) $k_x \approx 0.3677$ and (d) $k_x \approx 0.00785$. Parameter values are (a–c) $\phi^0 = 0.2$ and $H = 100$ (same as in figure 3), and (d) $\phi^0 = 0.5$ and $H = 50$ (same as in figure 7).

the line with open circles represents the variation of $2a^{(0)}$ with k_x (where $a^{(0)}$ corresponds to the least-stable mode as displayed in figure 16a), and the dashed horizontal line represents a real eigenvalue of the streamwise-independent flow (which is not the least-stable eigenvalue at $k_x = 0$ for this parameter set). Both the growth rate curves intersect at $k_x \approx 0.3677$, as shown by an arrow in figure 16(c), and this is the point at which the mean-flow resonance condition,

$$2a^{(0)}(k_x = 0.3677) = a_j^{(0)}(k_x = 0) \approx -8.56434 \times 10^{-3}, \qquad (6.7)$$

is exactly satisfied. In (6.7), $j = 11$, implying that the 11th mode (the ordering of modes is done by arranging them in descending order of their growth rates) of the streamwise-independent flow ($k_x = 0$) is responsible for the above mean-flow resonance, resulting in a kink on the $a^{(2)}$-curve in figure 16(b). The inset of figure 16(c) shows a zoomed variation of the first Landau coefficient that diverges and undergoes a sign change at the resonant wavenumber ($k_x \approx 0.3677$).

We now explain the divergence of $a^{(2)}$ at long waves in figure 7(b), for which the parameter values are $\phi^0 = 0.5$, $H = 50$ and $e = 0.8$. The corresponding variations of $2a^{(0)}(k_x)$ and $a^{(0)}(k_x = 0)$ are displayed in figure 16(d) by solid and dashed lines, respectively, which intersect at $k_x \approx 0.00785$. (The dashed line in figure 16d corresponds to the second shear-banding mode, $a_{j=2}^{(0)}(k_x = 0) \approx -2.97079 \times 10^{-6}$, which is stable;
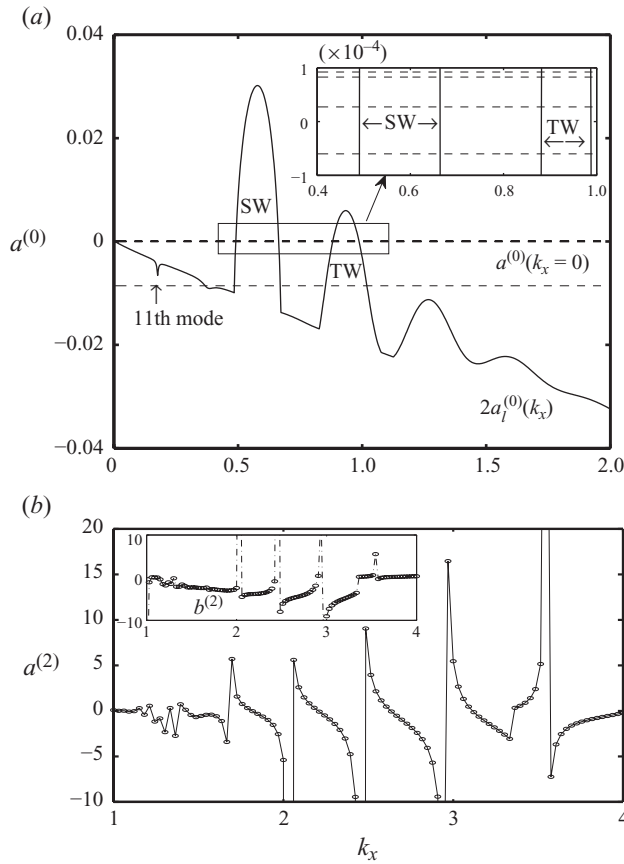
FIGURE 17. (a) Evidence of mean-flow resonance: variation of the real part of the least-stable mode $[2a^{(0)}(k_x)]$ with k_x at $\phi^0 = 0.2$, $H = 100$ and $e = 0.8$. The dashed horizontal lines refer to different shear-banding modes $k_x = 0$. The intersection points of dashed lines with the solid line denote the locations of k_x at which mean-flow resonance occurs as explained in the text. (b) Divergence of $a^{(2)}(k_x)$ for $k_x > 1$.

note that the 'leading' shear-banding mode is unstable at $\phi^0 = 0.5$ and $H = 50$: see figure 4.) Hence, there is a mean-flow resonance at $k_x \approx 0.00785$, which is responsible for the divergence of $a^{(2)}$ in figure 7(b).

In fact, such a mean-flow resonance (3.32) can occur at multiple locations at various values of k_x for a given set of parameters (ϕ^0, H, e). To demonstrate this, we replotted the growth rate curve of figure 3 in figure 17(a) by a solid line – recall that this corresponds to the parameter values ($\phi^0 = 0.2$, $H = 100$ and $e = 0.8$) of the square symbol in figure 4. We have also plotted five real eigenvalues of shear-banding modes (i.e. at $k_x = 0$) whose growth rates can be parametrized by wavenumber such that

$$2a^{(0)}(k_x) = a_j^{(0)}(0), \quad \forall \quad j = 1, 2, 3, \ldots, \tag{6.8}$$

shown by dashed horizontal lines in figure 17(a). In fact, the upper (thick) dashed line in figure 17(a) corresponds to the first four modes, $a_{j=1,2,3,4}^{(0)}(0) = 9.2125 \times 10^{-5}$, 8.28485×10^{-5}, 2.72077×10^{-5} and -5.99651×10^{-5}, which are very close to each other, as clarified in the zoomed inset. The first two (almost) vertical solid lines in the inset correspond to the zoomed version of the dominant stationary wave (SW)
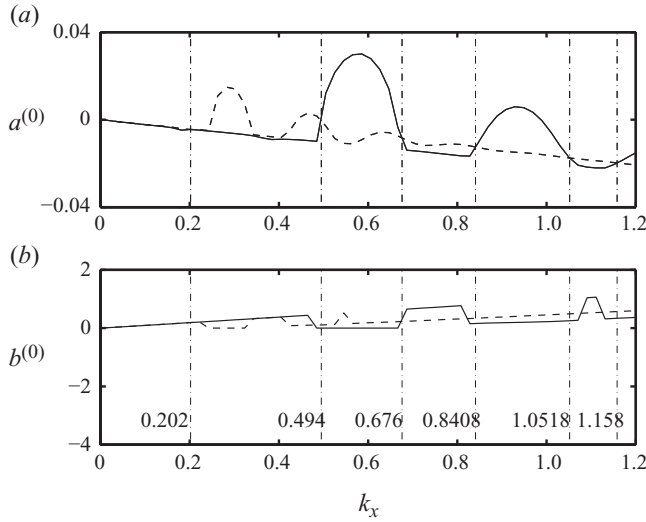
FIGURE 18. Possible onset of the $1:2$ resonance at $\phi^0 = 0.2$, $H = 100$ and $e = 0.8$: variation of (a) the real part, $a^{(0)}$, (b) the imaginary part, $b^{(0)}$, of the least-stable mode with k_x.

of figure 17(a) and the next two vertical lines correspond to travelling waves (TW). It is clear from this inset that the growth rates of these four shear-banding modes ($a^{(0)}(k_x = 0)$) coincide with the growth rates ($2a^{(0)}(k_x)$) of the dominant stationary and travelling waves, satisfying the mean-flow resonance condition (3.32) exactly at 16 different values of k_x (which are, of course, very close to each other). Consequently, there are multiple resonance points at various values of k_x, near the zero crossings of SW and TW. (That the first Landau coefficient diverges at such resonance points can be ascertained from figures 10(a) and 12(b).) The lower dashed line in figure 17(a) corresponds to the 11th shear-banding mode [$a^{(0)}_{j=11}(k_x = 0) = -8.56434 \times 10^{-3}$], which is responsible for the mean-flow resonance in figure 16(c). Note that in figure 17(a) the flow is linearly stable for large values of $k_x > 1$. However, there are multiple resonance points in this stable regime too, as implicated by the discontinuities on the curves of $a^{(2)}$ and $b^{(2)}$ at various values of k_x (see figure 17b), where the mean-flow resonance condition (3.32) is satisfied.

Now we discuss the possible occurrence of the $1:2$ resonance condition (3.34) in the present flow. While the solid line in figure 18(a) represents the variation twice of the growth rate of the least-stable mode, $2a^{(0)}_l(k_x)$, that in figure 18(b) represents the corresponding variation of frequency, $2b^{(0)}_l(k_x)$. The dashed lines in figure 18(a,b) represent the growth rate and frequency curves, parametrized by $a^{(0)}(k_x) = a^{(0)}_l(2k_x)$ and $b^{(0)}(k_x) = b^{(0)}_l(2k_x)$, respectively. The points of intersection of the solid and dashed lines in figure 18(a) are marked by vertical dot-dashed lines where the growth rates are equal. However, the $1:2$ resonance condition (3.34) is not satisfied at these points because while the condition on the growth rate,

$$2a^{(0)}_l(k_x) = a^{(0)}_l(2k_x), \tag{6.9}$$

is satisfied, the equality of frequencies does not hold, i.e.
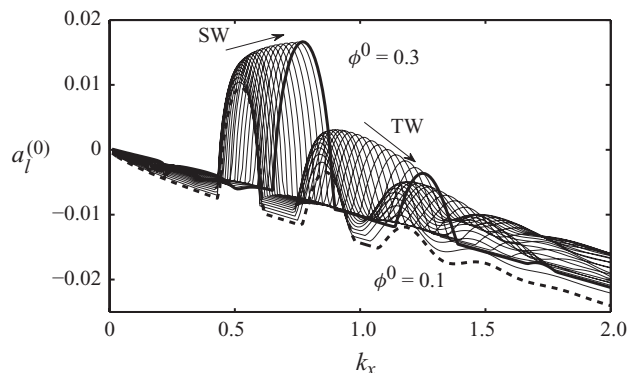
$$2b^{(0)}_l(k_x) \neq b^{(0)}_l(2k_x) \tag{6.10}$$

FIGURE 19. Effect of mean density on the growth rate of the least-stable mode at $H = 100$ and $e = 0.8$.

at these points. We have checked a few other parameter combinations, but could not find the occurrence of a $1:2$ resonance in this flow. We note in passing that the $1:2$ resonance between two travelling waves corresponds to a codimension-3 bifurcation point (Golubitsky & Schaffer 1985; Proctor & Jones 1988; Fujimura 1992), and therefore requires an exhaustive search in the parameter space which is not pursued further in this paper.

Irrespective of the types of resonance (i.e. mean flow or $1:2$), the first Landau coefficient is divergent at the resonance point. In the following sections, we will present results for $a^{(2)}$ and $b^{(2)}$, which contain such resonance points as implicated by discontinuities in the first Landau coefficient.

6.4. *Dominant stationary and travelling instabilities: effects of density and Couette gap*

We define the dominant eigenvalue as the one having the maximum growth rate over all wavenumbers for a specified control parameter combination of (H, ϕ^0, e). In other words, it is the supremum of all leading eigenvalues, as defined in (6.1), over all k_x:

$$a_l^d = \sup_{k_x} a_l^{(0)}. \tag{6.11}$$

The wavenumber corresponding to this dominant mode is referred to as the dominant wavenumber:

$$k_x^d = k_x(a^{(0)} = a_l^d). \tag{6.12}$$

For example, in figure 3, we have plotted the growth rate of the leading eigenvalue, $a_l^{(0)}$, with k_x at $(H, \phi^0) = (100, 0.2)$ and $e = 0.8$. The dominant mode for this parameter combination comes from the maximum of the growth rate curve that occurs at the first peak at $k_x \approx 0.5858$, which is a stationary wave; the second dominant mode corresponds to the maximum of the second peak at $k_x \approx 0.9349$ in figure 3, which is a travelling wave. Recall that the growth rates of these stationary and travelling instabilities, which appear at $k_x = O(1)$, are an order of magnitude larger than those appearing at long waves ($k_x \sim 0$: see §6.1). So far, we have presented results on these dominant instabilities at a mean density of $\phi^0 = 0.2$ and a Couette gap of $H = 100$ in §§6.2 and 6.3. In this section, we probe the effects of varying mean density and Couette gap on the nonlinear saturation of these dominant stationary and travelling instabilities.
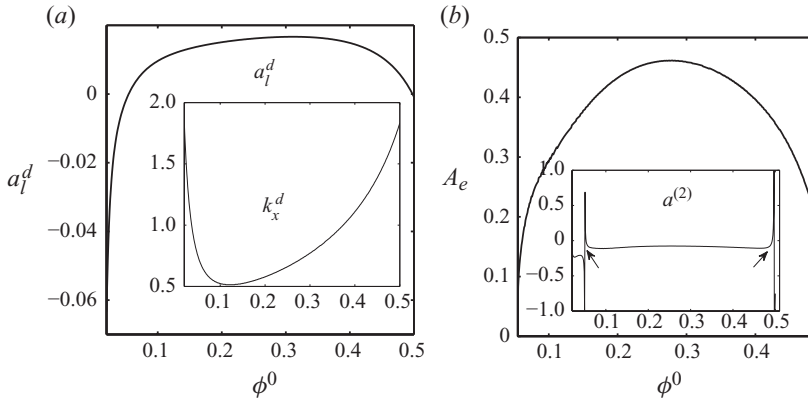
FIGURE 20. Effect of mean density on the dominant stationary instability, corresponding to the first peak in figure 19. (a) a_l^d (main panel) and k_x^d (inset); (b) supercritical/stable A_e (main panel) and $a^{(2)}$ (inset).

6.4.1. *Effect of mean density*

In figure 19, we show the variations of $a_l^{(0)}$ with k_x for 24 different mean densities ranging from $\phi^0 = 0.1$ to 0.3, with parameter values as in figure 3. The dashed and thick solid lines correspond to $\phi^0 = 0.1$ and 0.3, respectively, and the thin solid lines refer to the remaining equally spaced densities. For each density, the first dominant peak refers to stationary waves, and the next one to travelling waves. Note that the locations of both the dominant stationary and travelling wave peaks move to larger values of k_x with increasing density from $\phi^0 = 0.1$ to 0.3.

The variation of the growth rate of the above-discussed dominant stationary instability, a_l^d, with mean density is shown in figure 20(a), and the corresponding variation of the dominant wavenumber, k_x^d, is shown in its inset. It is seen that the dominant growth rate is maximum at an intermediate value of $\phi^0 \sim 0.3$ and decreases in both the dilute and dense limits. Also, the dominant wavenumber is minimum at $\phi^0 \sim 0.1$ and increases in both the dilute and dense limits, implying that the wavelength ($\lambda_x = 2\pi/k_x$) of the dominant instability is maximum at some intermediate density but decreases sharply in both dilute and dense limits. Within the density range over which the dominant stationary instability is unstable ($a_l^d > 0$), the first Landau coefficient $a^{(2)}$ is negative as seen in the inset of figure 20(b); the imaginary part of the first Landau coefficient $b^{(2)}$ is zero for stationary waves and hence not shown. (Note that the jumps in $a^{(2)}$, marked by arrows in the inset of figure 20b, correspond to the mean-flow resonance condition (3.32) being satisfied at those locations.) Therefore, at $H = 100$ (refer to the square symbol in figure 4), the supercritical (and hence stable) stationary solutions exist for a range of mean densities as shown in the main panel of figure 20(b). It has been verified that this range of ϕ^0, over which such nonlinear equilibrium states exist, becomes larger in wider Couette gaps (i.e. with increasing H).

With the finite amplitudes as in figure 20(b), the corresponding nonlinear stationary patterns of the perturbation density and velocity fields are displayed in figures 21(a, c, e) and 21(b, d, f), respectively, for three values of mean density: figures 21(a, b), 21(c, d) and 21(e, f) correspond to $\phi^0 = 0.1$, 0.3 and 0.45, respectively, with dominant wavenumbers $k_x^d = 0.52$, 0.77 and 1.39. These plots should also be compared with figure 11(a, e) for $\phi^0 = 0.2$. It is seen that the overall features of density
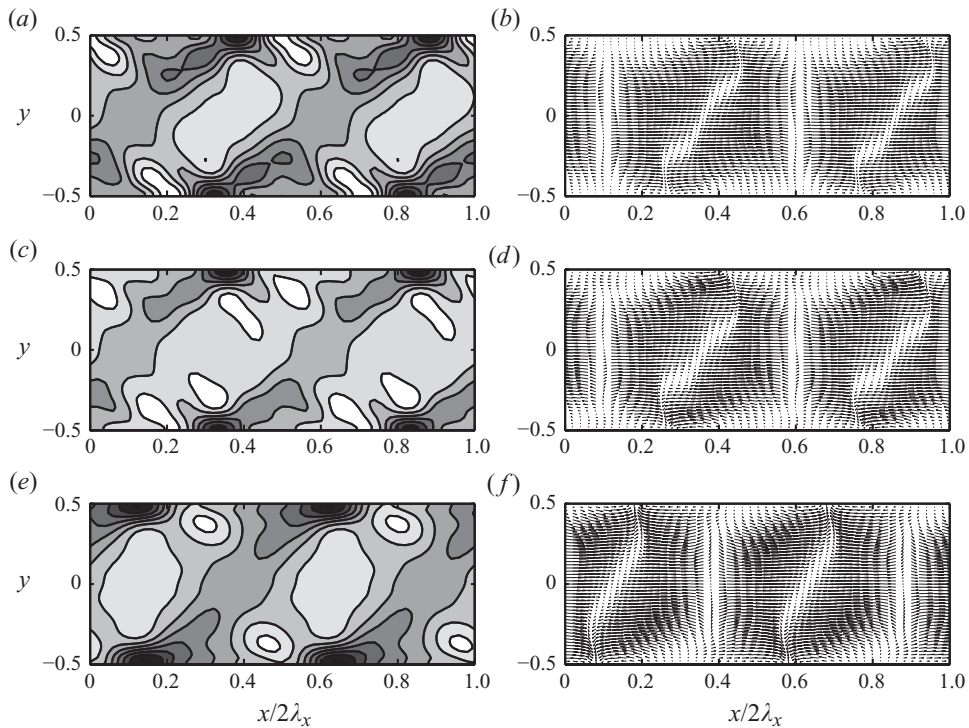
FIGURE 21. Effect of mean density on nonlinear patterns of perturbation density (a, c, e) and velocity (b, d, f) for the dominant stationary instability in figure 20: (a, b) $\phi^0 = 0.1$ $(k_x = 0.52)$, (c, d) $\phi^0 = 0.3$ $(k_x = 0.77)$ and (e, f) $\phi^0 = 0.45$ $(k_x = 1.39)$.

and velocity fields look similar at any mean density. Note further that the related plots of linear perturbations at $\phi^0 = 0.1$, 0.3 and 0.45 (not shown) look strikingly similar to those at $\phi^0 = 0.2$ as in figure 11(b, f). Therefore, the overall structural features of both linear and nonlinear perturbation fields for the dominant stationary instability remain relatively unaffected by variations in mean density, i.e. whether the flow is dilute $(\phi^0 = 0.1)$ or dense $(\phi^0 = 0.45)$.

For the dominant travelling wave, corresponding to the second peak in figure 19, the variations of a_l^d and c_{ph} with mean density ϕ^0 are shown by solid and dot-dashed lines, respectively, in figure 22(a). The phase velocity, c_{ph}, of the dominant travelling mode remains relatively unaffected with changes in mean density; however, its growth rate a_l^d is maximum at some intermediate density $\phi^0 \sim 0.2$ and decreases in both dilute and dense limits. The corresponding dominant wavenumber k_x^d, shown in the inset of figure 22(a), varies non-monotonically with ϕ^0 and is minimum at $\phi^0 \sim 0.1$ and increases in both dilute and dense limits. Comparing figure 22(a) with figure 20(a) we find that the growth rate and the unstable range of densities are much smaller for the dominant travelling wave than its stationary counterpart and so is its wavelength (since $\lambda_x \sim 1/k_x^d$).

The dominant travelling waves in figure 22(a) undergo 'supercritical' and 'subcritical' Hopf bifurcations over the density range of $\phi^0 \sim (0.12, 0.25)$ and $\phi^0 \sim (0.317, 0.343)$, respectively: see figures 22(b) and 22(c). The variations of the real part of the first Landau coefficient, $a^{(2)}$, and the growth rates are displayed in the insets of figures 22(b) and 22(c), and those of the equilibrium amplitude A_e and the
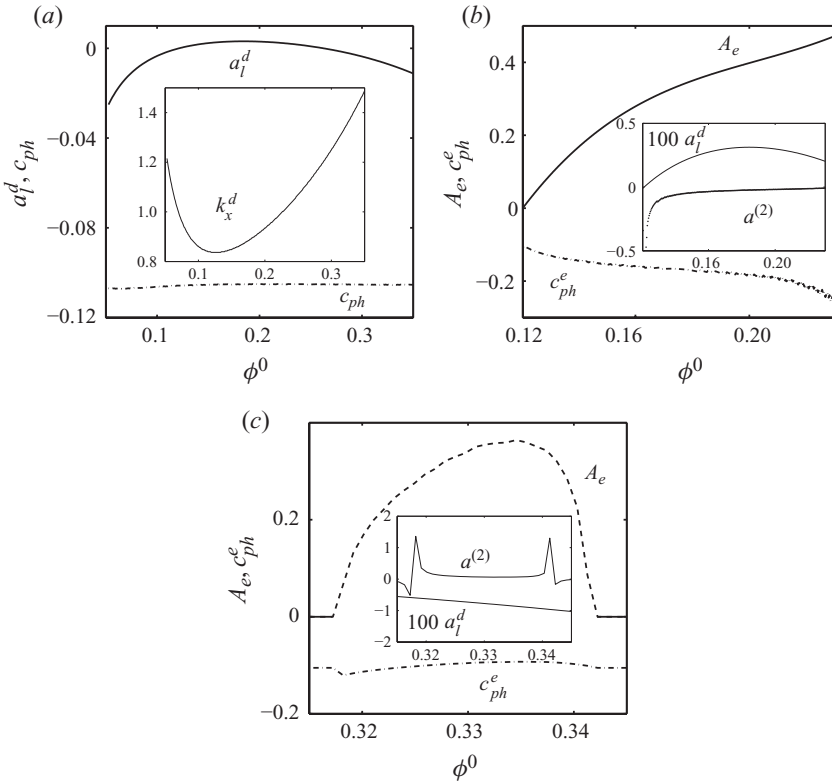
FIGURE 22. Effect of the mean density on the dominant travelling wave, corresponding to the second peak in figure 19. (*a*) a_l^d (solid line), its phase velocity (dot-dashed line) and k_x^d (inset); (*b*) supercritical/stable A_e, c_{ph}^e (main panel) and $a^{(0)}$ and $a^{(2)}$ (inset); (*c*) subcritical/unstable A_e, c_{ph}^e (main panel) and $a^{(0)}$ and $a^{(2)}$ (inset).

equilibrium phase velocity c_{ph}^e in their respective main panels. The nonlinear solution branches in figures 22(*b*) and 22(*c*) are responsible for 'stable' and 'unstable' limit cycles, respectively, similar to those in figures 12(*d*) and 14(*d*). Corresponding to an unstable limit cycle such as in figure 14(*d*), there exists a stable limit cycle of larger amplitude that requires the knowledge of the second Landau coefficient $c^{(4)}$ (which is not calculated here).

The nonlinear travelling patterns (at $t = 0$) of the perturbation density, granular temperature and velocity fields are shown in figure 23 – figures 23(*a*, *c*, *e*) and 23(*b*, *d*, *f*) correspond to stable and unstable solutions at $\phi^0 = 0.15$ and 0.33, respectively, with other parameters as in figure 22. It must be noted that the structural features of stable travelling solutions at any density over $\phi^0 \sim (0.12, 0.23)$ resemble those in figure 23(*a*, *c*, *e*) and the unstable solutions at any $\phi^0 \sim (0.317, 0.342)$ look similar to those in figure 23(*b*, *d*, *f*). It is clear from figure 23 that the stable and unstable nonlinear solutions for all three fields are markedly different from each other. More specifically, the unstable patterns support larger fluctuations in the (x, y)-plane in all fields than the corresponding stable patterns. This may be contrasted with the fact that the underlying linear fields for either case of supercritical and subcritical Hopf bifurcations look similar, such as those in figure 13(*b*, *d*, *f*).
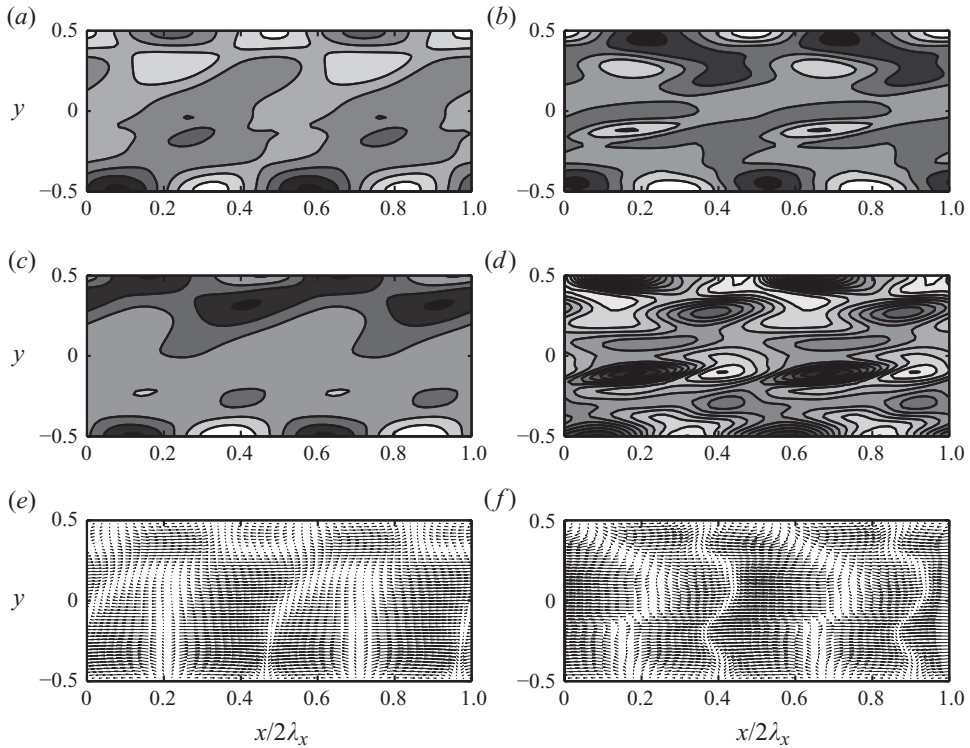
FIGURE 23. Nonlinear patterns of (a, b) density, (c, d) temperature and (e, f) velocity fields for the dominant travelling instability in figure 22 at two mean densities: (a, c, e) $\phi^0 = 0.15$ and $k_x = 0.84$ (stable); (b, d, f) $\phi^0 = 0.33$ and $k_x = 1.3$ (unstable).

6.4.2. *Effect of Couette gap*

The results in §6.4.1 pertain to a fixed Couette gap of $H = 100$ over a range of mean densities $\phi^0 \in (0.05, 0.5)$. Here, we fix the mean density at $\phi^0 = 0.2$ and probe the effect of varying Couette gaps on dominant instabilities, along the horizontal arrows in figure 4. Figure 24 shows the variation of the growth of the least-stable mode with k_x for a few values of $H \in (25, 100)$. It is seen that the dominant stationary instability at $H = 100$ (the first peak on the thick solid line) becomes stable for narrower Couette gaps (say, at $H = 25$, indicated by the dashed line in figure 24). Therefore, there is a minimum Couette gap $(H = H_c^{SW})$ below which the stationary instability with $k_x \sim O(1)$ becomes stable.

For the dominant instability, corresponding to the first peak in figure 24, we have shown the variations of its growth rate a_l^d with H and the corresponding first Landau coefficient $a^{(2)}$ (with $b^{(2)} = 0$) in figures 25(a) and 25(b), respectively. The flow is unstable to this instability for $H > 35.8$; the growth rate a_l^d reaches a maximum at some value of H (~ 70) and decreases slowly thereafter. The dominant wavenumber k_x^d decreases monotonically with increasing H (see the inset in figure 25a), and hence the corresponding wavelength increases. In fact, the dominant wavelength λ_x^d/d (in terms of particle diameter) increases from 20π to 1000π at $H = 25$ and 200, respectively, and $\lambda_x^d/\bar{h}$ from 0.8π to 5π in terms of the Couette gap. The inset in figure 25(b) displays a zoomed version of $a^{(2)}$ over a smaller range of H, and the two discontinuities in $a^{(2)}$
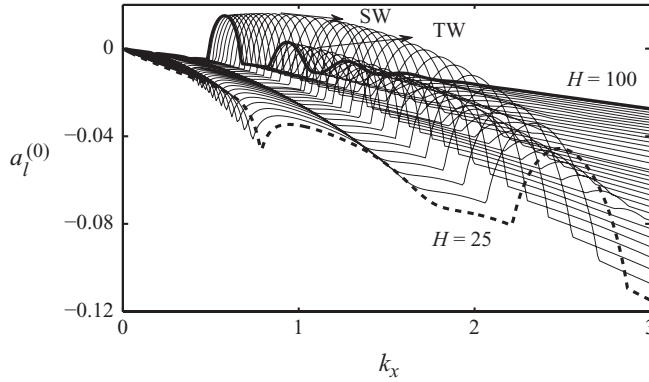
FIGURE 24. Effect of the Couette gap on the growth rate of the least-stable mode at $\phi^0 = 0.2$ and $e = 0.8$.
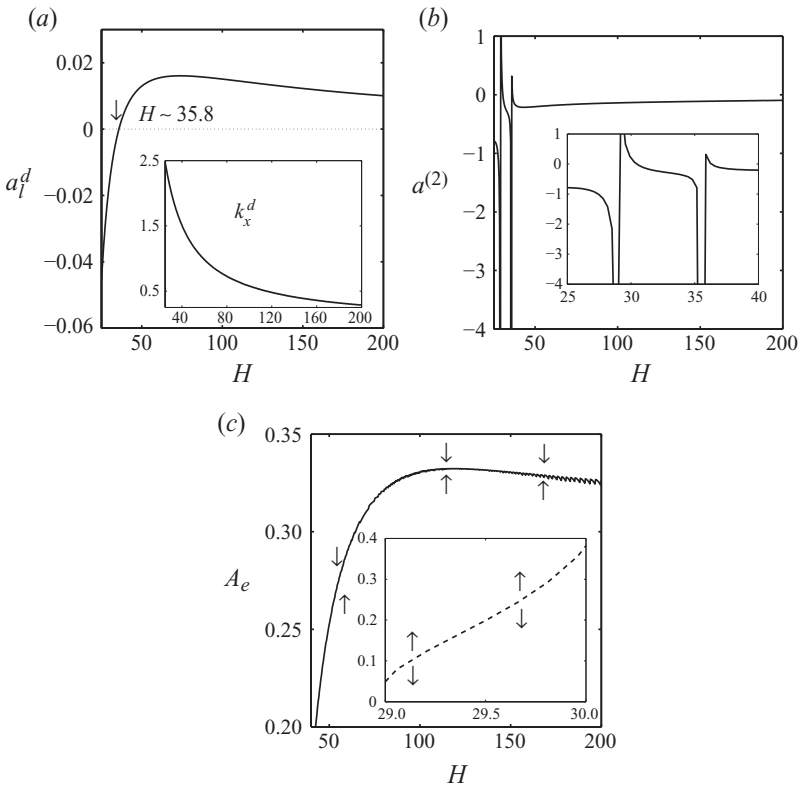

FIGURE 25. Effect of the Couette gap on the dominant stationary instability at $\phi^0 = 0.2$ and $e = 0.8$: (a) a_l^d (main panel) and k_x^d (inset); (b) $a^{(2)}$; (c) 'supercritical' equilibrium amplitude (main panel) for $H > 36$ and 'subcritical' amplitude (inset) for $H \in (29, 30)$.

at $H \sim 29$ and $H \sim 36$ correspond to the mean-flow resonance condition (3.32) being satisfied there.

For the dominant stationary instability in figure 25(a), the nonlinear solutions appear via 'supercritical' pitchfork bifurcations for a large range of Couette gaps $H \in (36, 100)$ as shown in the main panel of figure 25(c). However, the 'subcritical'
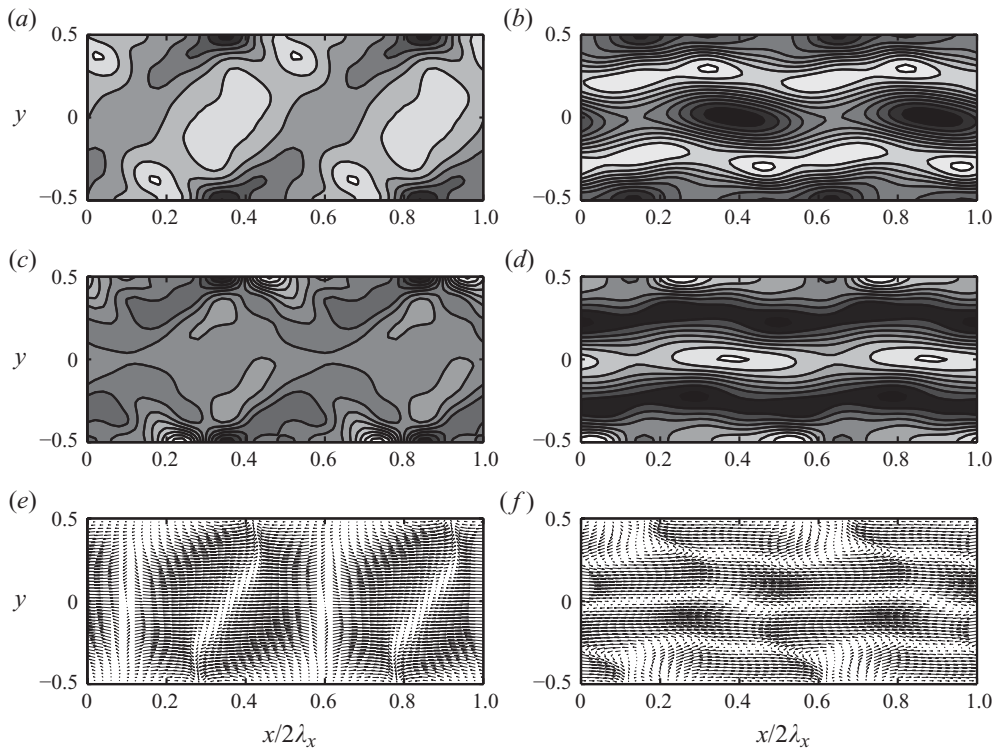
FIGURE 26. Effects of the Couette gap on the nonlinear patterns of density (a, b), granular temperature (c, d) and velocity (e, f) for the dominant stationary instability in figure 25: (a, c, e) $H = 50$ and $k_x = 1.18$ (stable solution) and (b, d, f) $H = 30$ and $k_x = 2.05$ (unstable solution).

solutions also exist but for a very narrow range of Couette gaps $H \in (29, 30)$ as in the inset of figure 25(c). Note that in the inset of figure 25(b), $a^{(2)}$ is positive for $H \in (29, 30)$, leading to subcritical bifurcations.

For parameter values of figure 25, the stable/supercritical nonlinear solutions at any $H \in (36, 100)$ look similar. This can be verified by comparing a representative stationary-wave solution for the patterns of density, granular temperature and velocity as displayed in figure 26(a, c, e) at a Couette gap of $H = 50$ (with other parameters as in figure 25) with figure 11(a, c, e) at $H = 100$. However, the unstable/subcritical solution at $H = 30$ looks completely different as shown in figure 26(b, d, f). (Note that the height and length ratios between two sets of images in figures 26(a, c, e) and 26(b, d, f) must be set proportional to $H_1/H_2 = 5/3$ and $L_{x1}/L_{x2} = k_{x2}/k_{x1} \approx 1.75$, respectively, for a fair comparison.) In the latter case, the particle bands/clusters are wavy and aligned primarily along the streamwise direction, which is in contrast to oblique clusters observed for stable/supercritical solutions in figure 26(a, c, e). The density field in figure 26(b) has some resemblance to the sinuous stationary mode found in particle simulations of Conway *et al.* (2006). (The solution for the corresponding stable branch, which requires the second Landau coefficient, is expected to remain similar since it represents a continuation of the unstable branch: see figure 2f.)

The effect of the Couette gap on the dominant travelling instability, corresponding to the second peak on the thick solid line in figure 24, has been studied at $\phi^0 = 0.2$ for a range of $H \in (25, 200)$, but we do not show these results, for the sake of
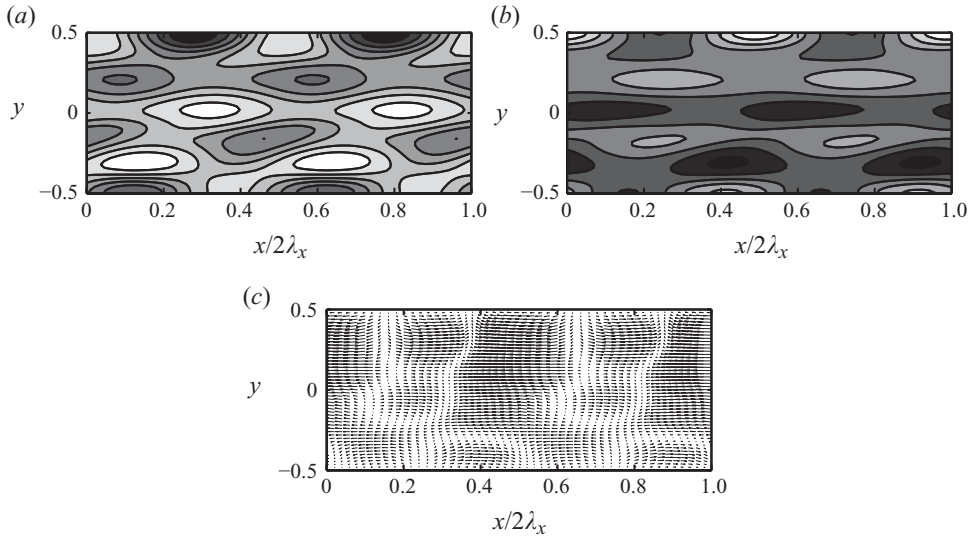
FIGURE 27. Nonlinear travelling patterns ($t = 0$) of (*a*) density, (*b*) temperature and (*c*) velocity field for the subcritical solution at $H = 80$, $\phi^0 = 0.2$, $e = 0.8$ and $k_x = 1.1$.

brevity. We found that the flow is linearly unstable to the dominant travelling instability (i.e. $a_l^d > 0$) beyond $H = H_c^{TW} \sim 85.5$. Here too we have subcritical and supercritical Hopf bifurcations over $H \in (78.5, 85.5)$ and $H > 85.5$, respectively. Over the subcritical range $H \in (78.5, 85.5)$, the flow is found to be susceptible to the mean-flow resonance (since this range of H belongs to the stable regime where the shear-banding modes, which participate in creating the mean-flow resonance, exists, see § 6.3) at different values of H. The patterns of stable/supercritical nonlinear travelling-wave solutions at $H > 85.5$ (not shown) look similar to those for $H = 100$, as displayed in figure 13. In contrast, the unstable/subcritical nonlinear solution at $H = 80$, shown in figure 27 (compare with figure 13*a*,*c*,*e*), looks markedly different from supercritical solution, even though the underlying linear perturbation fields (i.e. the eigenfunction or the fundamental mode) are similar in both cases. From the density and temperature contours in figure 27(*a*,*b*), we find that there are two additional rows of clusters in the bulk along with wall clusters, and the density bands are aligned along the streamwise direction.

6.5. *Effect of restitution coefficient*

So far, we have presented all results for a single restitution coefficient of $e = 0.8$, and this was done in continuation of previous linear stability results (Alam & Nott 1998) and nonlinear shear-banding results (Shukla & Alam 2011) of the same problem. It is of interest to know how the values of e, which is a measure of inelastic dissipation in a granular fluid, would affect the nonlinear saturation of dominant stationary and travelling wave instabilities. Here, we present brief results at a mean density of $\phi^0 = 0.2$ and a Couette gap of $H = 500$, focusing on a restitution coefficient of $e = 0.95$ that belongs to the quasi-elastic limit ($e \sim 1$).

For $e = 0.95$, $\phi^0 = 0.2$ and $H = 500$, figures 28(*a*) and 28(*b*) show the variations with k_x of the least-stable growth rate $a_l^{(0)}$ and its phase velocity c_{ph}, and the real part of the first Landau coefficient $a^{(2)}$, respectively. As explained in § 6.3, the discontinuities on the $a^{(2)}$-curve in figure 28(*b*) signal the onset of mean-flow resonance (3.32). The first peak on the growth rate curve in figure 28(*a*) corresponds to the dominant
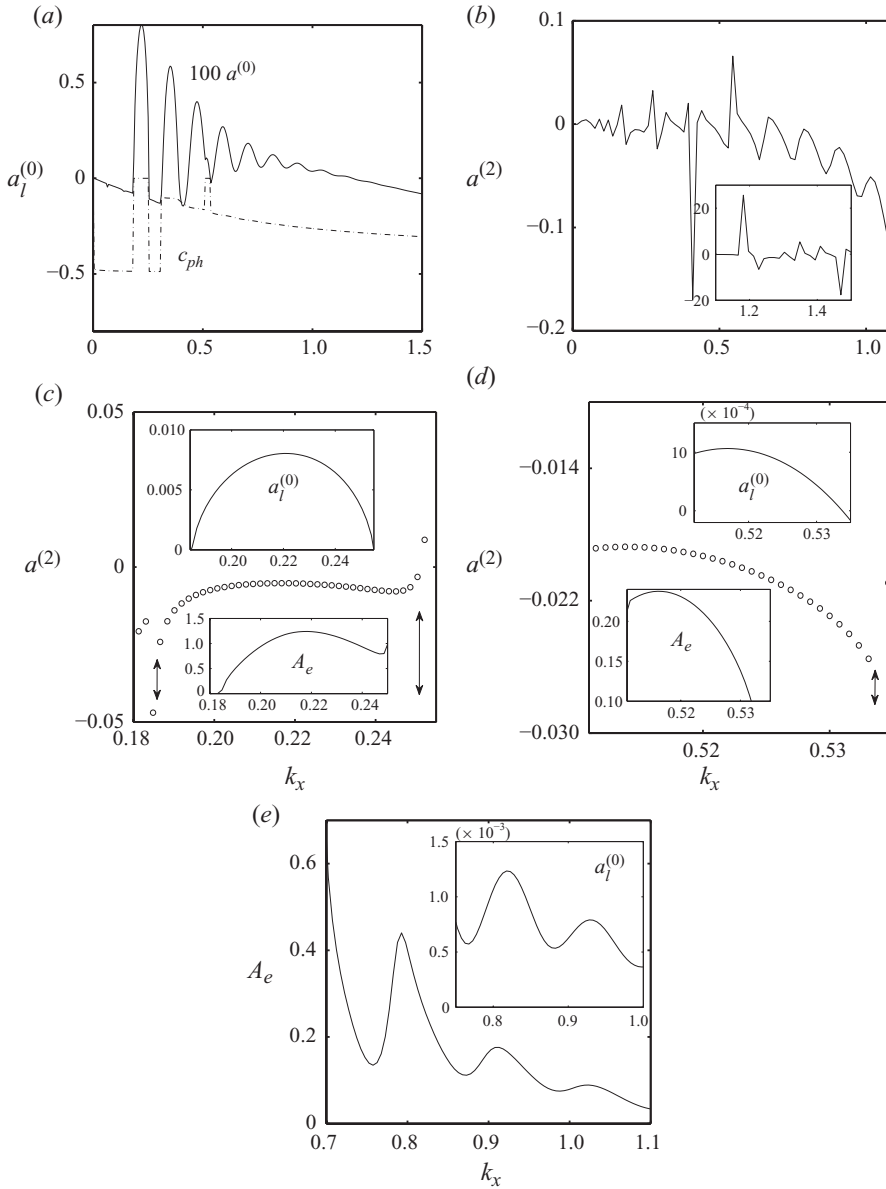
FIGURE 28. (*a–e*) Results in the quasi-elastic limit ($e = 0.95$) for a very large Couette gap $H = 500$ at $\phi^0 = 0.2$. See text for details.

stationary ($c_{ph} = 0$: see dot-dashed line) instability since the global maximum of $a_l^{(0)}$ over all k_x belongs to this peak; see the upper inset in figure 28(*c*) for a zoomed view of this peak which is located at $k_x \sim 0.22$. The second peak of the $a_l^{(0)}$-curve belongs to the dominant travelling ($c_{ph} \neq 0$) instability. The rest of the growth rate curve in figure 28(*a*) for even larger values of k_x belongs to travelling waves too, except for a small window of $k_x \sim (0.51, 0.535)$, over which the least-stable mode is stationary; see the corresponding variation of $a_l^{(0)}$ in the upper inset of figure 28(*d*).
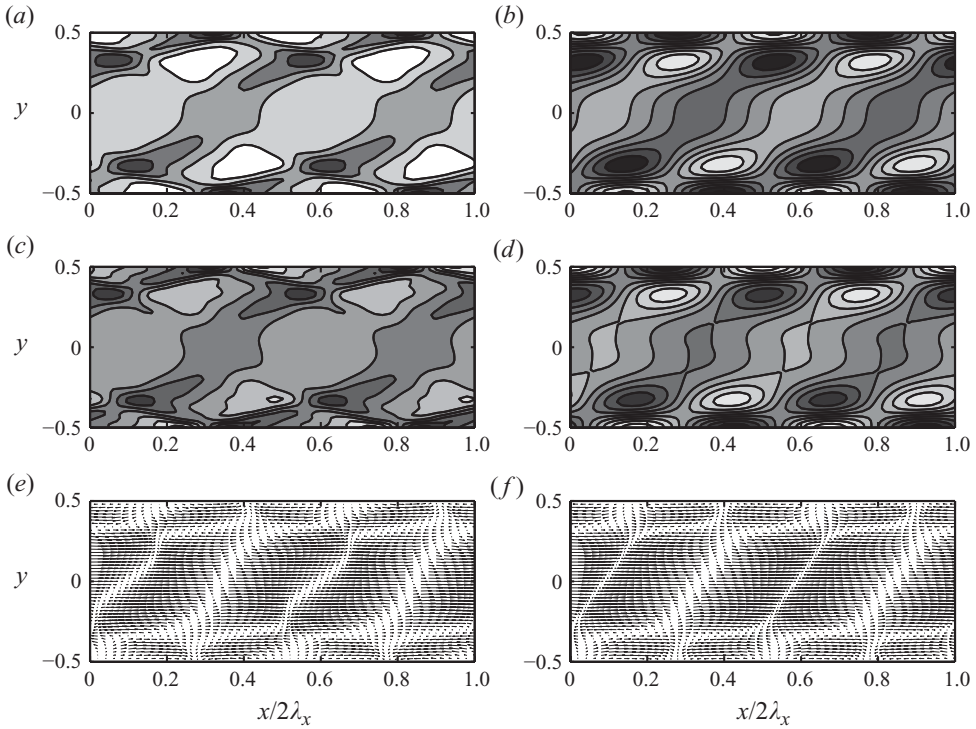
FIGURE 29. Nonlinear (a, c, e) and linear (b, d, f) 'stationary' patterns of (a, b) density, (c, d) temperature and (e, f) velocity fields in the (x, y)-plane. Parameter values are $H = 500$, $e = 0.95$, $\phi^0 = 0.2$ and $k_x = 0.517$, as in figure 28(d).

The variations of $a^{(2)}$ and the equilibrium amplitudes A_e for the above two stationary instabilities are displayed in the main panel and the lower inset, respectively, of figures 28(c) and 28(d). For both cases, we have supercritical pitchfork bifurcations since $a^{(0)} > 0$ and $a^{(2)} < 0$. The vertical double arrows in figures 28(c) and 28(d) correspond to k_x-values at which $a^{(2)}$ suffers a jump discontinuity due to the mean-flow resonance. From the lower insets of figures 28(c) and 28(d), we find that $A_e(k_x \approx 0.22)$ is about five times larger than $A_e(k_x \approx 0.517)$. Therefore, the nonlinear saturation of the 'second-type' stationary instability (at larger k_x) is more likely to occur than the dominant stationary instability (at smaller k_x), even though the growth rate of the former is smaller than that of the latter by about an order of magnitude (compare upper insets in figures 28c and 28d).

The nonlinear and linear disturbance patterns for the dominant stationary instability, corresponding to the first peak in figure 28(a), resemble those in figure 11 at $e = 0.8$ and $H = 100$, and hence we do not show them here. However, we focus on patterns for the 'new' stationary waves in figure 28(d) at $k_x = 0.517$ (with maximum growth rate). The corresponding nonlinear and linear patterns of perturbation density, granular temperature and velocity field are displayed in figures 29(a, c, e) and 29(b, d, f), respectively. A comparison between the linear density eigenfunctions in figures 11(b) and 29(b) suggests that the latter mode has two additional rows of particle clusters near two walls, the signature of which is also evident in the temperature and velocity maps as in figure 29(d, f). Therefore, this is a 'new' stationary instability which is structurally different (from that in figure 11) and that appears only in wider
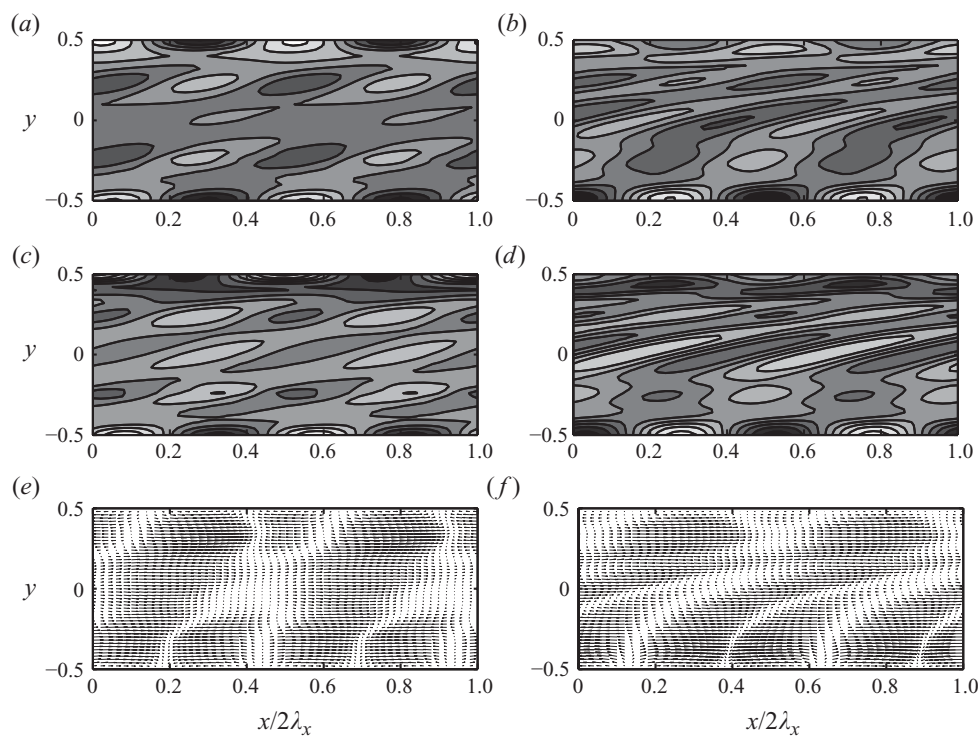
FIGURE 30. Nonlinear patterns of the travelling instability at (a, c, e) $k_x = 0.75$ and (b, d, f) $k_x = 1.0$. Parameter values are the same as in figure 28.

Couette cells of large H. The corresponding nonlinear patterns also look different, as seen in figures 29(a, c, e) and 11(a, c, e).

We have checked that the above-discussed new stationary mode persists at other values of e as long as the Couette gap H is large enough. More specifically, reducing the restitution coefficient e leads to the appearance of this new stationary instability in a system with a smaller Couette gap ($H < 500$), with other parameters being fixed as in figure 28.

With parameters as in figure 28(a), the variations of A_e for larger values of k_x are shown in figure 28(e) over which supercritical Hopf bifurcations occur: see the corresponding zoomed variation of $a^{(0)} > 0$ in the inset of figure 28(e) and that of $a^{(2)} < 0$ in the main panel of figure 28(b). For these travelling waves too, A_e decreases with increasing k_x. We show a comparison between the nonlinear patterns at $k_x = 0.75$ and 1.0 in figures 30(a, c, e) and 30(b, d, f), respectively. Both represent backward-travelling waves – note that the lengths of images in both columns should be proportional to the ratio of their wavelengths ($\lambda_{x1}/\lambda_{x2} = k_{x2}/k_{x1} = 4/3$). The patterns of density, temperature and velocity at $k_x = 1$ are more stretched and tenuous around the centreline compared with those at $k_x = 0.75$, but their structures near two walls look similar. The overall structural features of the pattern at $k_x = 1$ have some resemblance to the corresponding dominant travelling wave pattern: see figure 13(a, c, e).

6.6. *Discussion and qualitative comparison with molecular dynamic simulations*

It is important to pinpoint how the present results of a variety of nonlinear states in the granular plane Couette flow can be realized if we carry out particle simulations or direct simulations of full nonlinear hydrodynamic equations. Since our theory is

based on the assumption of streamwise periodicity (characterized by a wavenumber of $k_x = 2\pi/\lambda_x$, with its wavelength being λ_x: see (5.3)) and no-slip boundary conditions, simulations with similar restrictions should be able to capture the qualitative features of predicted patterns. For example, molecular dynamic simulations of inelastic hard disks with Lees–Edward boundary conditions (Alam & Luding 2003, 2005; Conway & Glasser 2004) should be able to capture nonlinear patterns. We have found that the predicted patterns correspond to streamwise wavenumbers of $k_x = O(1)$ or less (see figures 19 and 24), and hence the simulations must be performed in a rectangular box ($l_x > l_y$: see figure 1) since a square box corresponds to a streamwise wavenumber of $k_x = 2\pi$ (cf. (5.3)) for which the uniform shear flow remains stable. Moreover, the box length along the x-direction (refer to figure 1) should be chosen such that it admits at least one wavelength of the corresponding nonlinear pattern (i.e. $l_x \geqslant \lambda_x$: see (5.3) and (6.4)).

As mentioned in §1.2, the most comprehensive particle simulation to track instabilities in a granular shear flow was carried out by Conway & Glasser (2004) in a rectangular box. They used sink-type and slip boundary conditions so as to verify certain instabilities predicted by the linear stability theory of Alam & Nott (1998). Hence, a direct comparison between present results (with no-slip and adiabatic walls) and simulations of Conway & Glasser is not possible. Even though the structural features of some nonlinear patterns appear to be different from those found in simulations of Conway & Glasser, certain features of our predictions agree qualitatively with their simulations as we discuss below. Also, some of our density patterns might be related to the tenuous structures of 'churn-type' flow in the simulations of Tan & Goldhirsch (1997).

Conway & Glasser (2004) reported the appearance of two-dimensional stationary waves in dilute flows when the Couette gap H was large enough (refer to their phase diagram of different patterns in figure 17). Now, our nonlinear theory predicts (refer to figures 4, 19 and 20) that there are 'supercritical' stationary waves with $k_x = O(1)$ as well as 'subcritical' shear-banding solutions ($k_x = 0$) in dilute flows. Note that the subcritical instabilities require *a priori* presence of 'finite' amplitude perturbations of specific types, but the supercritical instabilities can grow from 'infinitesimal' perturbations. Therefore, in the absence of any biased forcing, as per our theory the two-dimensional stationary waves are likely to prevail in dilute flows, which agrees with simulations of Conway & Glasser.

At larger mean densities (say, $\phi^0 > 0.2$), the two-dimensional stationary and travelling waves (figure 19) with $k_x = O(1)$ coexist with shear-banding ($k_x = 0$) and long-wave ($k_x \sim 0$) instabilities (figure 5a). Since all instabilities at $\phi^0 = 0.2$ (refer to the square symbol in figure 4) belong to 'supercritical' states, each can evolve from 'infinitesimal' perturbations with respective growth rate. Therefore, we have a competition among different instability modes and it is interesting to determine which mode is likely to eventually prevail. Comparing figure 5(a) with figure 19, we find that the growth rates of long-wave instabilities are about two orders of magnitude lower than those of the dominant stationary and travelling waves. Also, the growth rates of stationary waves with $k_x = O(1)$ are much larger than the corresponding travelling waves. Therefore, the dominant stationary waves with $k_x = O(1)$ are likely to emerge as the prevailing nonlinear patterns at $\phi^0 = 0.2$ and $H = 100$ if the channel length is such that the flow admits all four types of instabilities. This observation also agrees with simulations of Conway & Glasser (see their figure 17).

Referring to figures 20(a) and 22(a), we note that the growth rates of dominant stationary and travelling waves decrease with increasing mean density ($\phi^0 > 0.25$) and both eventually become stable in dense flows; however, the 'supercritical' shear-banding and long-wave instabilities still exist at much higher densities (see figure 4). This implies that the shear-banding-type patterns would prevail in dense flows if the Couette gap is kept fixed (say, at $H = 100$). At large enough Couette gaps ($H > H_c^{SW}$, where H_c^{SW} is the minimum Couette gap beyond which the dominant stationary instabilities appear), therefore, we are likely to observe a transition from two-dimensional stationary waves at dilute-to-moderate densities to shear-banding solutions in denser flows. This transition scenario has been verified in figure 17 by Conway & Glasser.

Lastly, for specific combinations of ϕ^0, H and k_x, it is possible that the dominant stationary and travelling wave instabilities may have comparable growth rates. This is a special case in which the present theory of a single Landau equation is unlikely to hold since our assumption of time-scale separation between critical and non-critical modes (see §3) breaks down. In such a scenario, the final pattern selection can be probed via the theory of mode interactions for which coupled Landau equations need to be derived (Proctor & Jones 1988; Manneville 1990). Clearly, much research needs to be carried out in this direction in future, focusing on different types of prototypical granular shear flows.

7. Conclusions and outlook

We have developed an order-parameter theory to describe the nonlinear periodic patterns in a two-dimensional granular plane Couette flow which is known to be linearly unstable to a variety of stationary and travelling instabilities, having modulations in both streamwise (x) and gradient (y) directions. This is the first nonlinear study of its kind in the literature of granular fluids for spatially inhomogeneous two-dimensional patterns. The related order-parameter equation, the Landau–Stuart equation, has been derived using the amplitude expansion method (Stuart 1960; Watson 1960) of nonlinear stability theory, extending our previous work (Shukla & Alam 2009, 2011) on one-dimensional shear-banding instability. The nonlinear stability of two classes of modes (in different regimes of streamwise wavenumber k_x) in the granular plane Couette flow has been studied in detail using the present order-parameter theory. The numerical results, obtained by employing a spectral-based numerical method, are presented for the first Landau coefficient, the equilibrium amplitude, the equilibrium phase velocity, the limit cycle and the nonlinear perturbation fields. The supercritical and subcritical regimes of both pitchfork/static and Hopf/oscillatory bifurcations have been identified, and the first evidence of two-dimensional nonlinear equilibrium states for stationary and travelling waves has been found in the granular plane Couette flow.

In addition to the well-known shear-banding instability ($k_x = 0$) whose nonlinear saturation has been studied recently by us (Shukla & Alam 2009, 2011), there are long-wave ($k_x \sim 0$) stationary and travelling instabilities in a granular plane Couette flow. For such long-wave modes, we have uncovered nonlinear equilibrium states of stationary waves in the dilute limit (where the flow is known to be stable to the shear-banding mode) and of both stationary and travelling waves at moderate-to-large densities. While the nonlinear solutions in the dilute limit appear via a subcritical pitchfork bifurcation, those at larger densities appear via supercritical pitchfork and Hopf bifurcations. From a comparison between linear and nonlinear

perturbation fields, we found that the origin of nonlinear states at $k_x \sim 0$ is tied to the corresponding 'subcritical'/'supercritical' nonlinear shear-banding solutions ($k_x = 0$).

There are stationary and travelling instabilities at moderate values of wavenumber $k_x \sim O(1)$ whose growth rates are larger than those at long waves by an order of magnitude or more: these are referred to as 'dominant' instabilities (see, for example, two dominant peaks at $k_x \sim 0.6$ and $k_x \sim 0.95$ in figure 3) in a granular plane Couette flow. For the dominant stationary instability, we found that the nonlinear solutions appear via supercritical pitchfork bifurcations (figures 20 and 25) over a range of mean densities (ϕ^0) at sufficiently large Couette gaps ($H > H_c^{SW}$) and this range of unstable ϕ^0 increases with increasing H; in the linearly stable regime ($H < H_c^{SW}$) there could be subcritical bifurcations (figure 25c). The nonlinear stationary patterns have density bands that are located at some oblique angle to the streamwise direction (figure 21). The structural features of supercritical stationary solutions look similar at any value of ϕ^0 and H, but the related unstable subcritical solutions are markedly different (having density bands parallel to the streamwise direction) from their supercritical counterparts, even though the linear eigenfunctions are similar for both cases.

For the dominant travelling instability, the flow is linearly unstable for a range of mean densities if the Couette gap is sufficiently large ($H > H_c^{TW} > H_c^{SW}$), and there are subcritical nonlinear travelling waves at $H < H_c^{TW}$ at a given ϕ^0. For $H > H_c^{TW}$, there are supercritical and subcritical Hopf bifurcations at small and large values of ϕ^0 (figure 22), respectively; the latter finding of subcritical travelling solutions at moderate-to-large densities is in contrast to supercritical solutions for the dominant stationary mode. The supercritical and subcritical solutions look structurally different for the dominant travelling waves too. In addition to dominant travelling wave instability, there are linearly stable travelling waves at $k_x \sim O(1)$ which could also be unstable with respect to finite-amplitude disturbances (figure 14).

The effect of restitution coefficient on the nonlinear saturation of dominant instabilities has been studied. We found that the structural features of the nonlinear stationary and travelling wave solutions remain unaffected by the level of inelastic dissipation as long as the underlying linear eigenfunctions are similar. We have uncovered a new stationary instability in a very wide Couette cell ($H = 500$), which seems to persist at any restitution coefficient ($e \neq 1$), and the equilibrium amplitude A_e required to attain this mode is much smaller than the corresponding 'dominant' stationary instability. Apart from providing the first evidence of a variety of two-dimensional nonlinear patterns in a granular plane Couette flow, we hope that the present work will inspire large-scale particle simulations to detect such stable and unstable nonlinear states in the granular plane Couette flow as discussed briefly in §6.6.

By analysing the modal equations at quadratic order in perturbation amplitude, we have identified two types of nonlinear resonances: (i) the 'mean-flow' resonance and (ii) the '1 : 2' resonance. The former occurs due to the interaction of least-stable mode at some $k_x \neq 0$ with a shear-banding mode ($k_x = 0$), obeying the following condition on growth rate [$a^{(0)}$] and frequency [$b^{(0)}$]: $2a_\alpha^{(0)}(k_x) = a_\beta^{(0)}(k_x = 0)$ and $b_\beta^{(0)}(k_x = 0) = 0$, where α and β refer to two interacting modes. The 1 : 2 resonance occurs due to the interaction of two modes α and β, obeying $2a_\alpha^{(0)}(k_x) = a_\beta^{(0)}(2k_x)$ and $2b_\alpha^{(0)}(k_x) = b_\beta^{(0)}(2k_x)$, with their wavenumber ratio being 1 : 2. The signature of either type of resonances is implicated by the divergence of the first Landau coefficient at specific values of wavenumber k_x where the resonance takes place. Our numerical results in §6.3 have clearly demonstrated the existence of mean-flow resonance in a granular plane

Couette flow; however, the existence of the $1:2$ resonance remained elusive in the present flow. Note that the $1:2$ resonance points, being codimension-3 bifurcation points, require an exhaustive search in the parameter space to locate them, which has not been pursued in this paper.

It must be noted that the present nonlinear analysis using a single Landau equation is not valid near resonance points. For parameter values at which such mode interactions occur, we need to include the amplitudes of all interacting modes in the perturbation method and this leads to a coupled set of Landau equations (Mizushima & Gotoh 1985; Proctor & Jones 1988; Manneville 1990; Fujimura 1992). The detailed perturbation method and the bifurcation analysis for resonating modes and the coupled Landau equations are left to future work. The present order-parameter theory can be used to probe the bifurcation and pattern-formation scenario in a host of granular flow problems, namely granular Faraday waves (Umbanhower, Melo & Swinney 1996), granular Rayleigh–Bénard convection (Khain & Meerson 2003; Eshuis *et al.* 2010), granular Poiseuille flow (Raafat, Hulin & Herrmann 1996; Alam, Chikkadi & Gupta 2009), Kelvin–Helmholtz instability (Goldfarb *et al.* 2002) and inclined chute flow of granular materials (Forterre & Pouliquen 2002). Work in this direction is in progress.

REFERENCES

ALAM, M. 2006 Streamwise structures and density patterns in rapid granular Couette flow: a linear stability analysis. *J. Fluid Mech.* **553**, 1–32.

ALAM, M., ARAKERI, V. H., GODDARD, J., NOTT, P. R. & HERRMANN, H. J. 2005 Instability-induced ordering, universal unfolding and the role of gravity in granular Couette flow. *J. Fluid Mech.* **523**, 277.

ALAM, M., CHIKKADI, V. K. & GUPTA, V. K. 2009 Density waves and the effect of wall roughness in granular Poiseuille flow: simulation and linear stability. *Eur. Phys. J. ST*, **179**, 69.

ALAM, M. & LUDING, S. 2003 First normal stress difference and crystallization in a dense sheared granular fluid. *Phys. Fluids* **15**, 2298.

ALAM, M. & LUDING, S. 2005 Energy non-equipartition, rheology and microstructure in sheared bidisperse granular mixtures. *Phys. Fluids* **17**, 063303.

ALAM, M. & NOTT, P. R. 1998 Stability of plane Couette flow of a granular material. *J. Fluid Mech.* **377**, 99.

ALAM, M. & SHUKLA, P. 2008 Nonlinear stability of granular shear flow: Landau equation, shear-banding and universality. In *Proc. Intl Congress on Theoretical and Applied Mechanics*: ICTAM 2008 (ed. E. Tuck), Adelaide, Australia.

ALAM, M., SHUKLA, P. & LUDING, S. 2008 Universality of shear-banding instability and crystallization in sheared granular fluid. *J. Fluid Mech.* **615**, 293.

ARANSON, I. S. & TSIMRING, L. S. 2006 Patterns and collective behaviour in granular media: theoretical concepts. *Rev. Mod. Phys.* **78**, 641.

BRILLIANTOV, N. & PÖSCHEL, T. 2004 *Kinetic Theory of Granular Gases.* Oxford University Press.

BUSSE, F. H. 1978 Nonlinear properties of thermal convection. *Rep. Prog. Phys.* **41**, 1929.

CANUTO, C., HUSSAINI, M. Y., QUARTERONI, A. & ZANG, T. A. 1988 *Spectral Methods in Fluid Dynamics.* Springer.

CONWAY, S. L. & GLASSER, B. J. 2004 Density waves and coherent structures in granular Couette flow. *Phys. Fluids* **16**, 509.

CONWAY, S. L., LIU, X. & GLASSER, B. J. 2006 Instability-induced clustering and segregation in high-shear Couette flows of model granular materials. *Chem. Engng Sci.* **61**, 6404.

CROSS, M. C. & HOHENBERG, P. C. 1993 Pattern formation outside of equilibrium. *Rev. Mod. Phys.* **65**, 851.

ECKHAUS, W. 1965 *Studies in Nonlinear Stability Theory.* Springer.

ESHUIS, P., VAN DER MEER, D., ALAM, M., VAN GERNER, H. J., VAN DER WEELE, K. & LOHSE, D. 2010 Onset of convection in strongly shaken granular matter. *Phys. Rev. Lett.* **104**, 038001.

FORTERRE, Y. & POULIQUEN, O. 2002 Stability analysis of rapid granular chute flows: formation of longitudinal vortices. *J. Fluid Mech.* **467**, 361.

FUJIMURA, K. 1992 Higher harmonic resonances in free convection between vertical parallel plates. *Proc. R. Soc. Lond.* A **340**, 95.

GAYEN, B. & ALAM, M. 2006 Algebraic and exponential instabilities in a sheared micropolar granular fluid. *J. Fluid Mech.* **567**, 195.

GOLDFARB, D. J., GLASSER, B. J. & SHINBROT, T. 2002 Shear instabilities in granular flows. *Nature* **415**, 302.

GOLUBITSKY, M. & SCHAEFFER, D. G. 1985 *Singularities and Groups in Bifurcation Theory,* vol. 1. Springer.

GUBA, P. & WORSTER, M. G. 2010 Interactions between steady and oscillatory convection in mushy layers. *J. Fluid Mech.* **645**, 411.

HOPKINS, M. A. & LOUGE, M. Y. 1991 Inelastic microstructures in rapid granular flows of smooth disks. *Phys. Fluids* A **3**, 47.

KHAIN, E. 2007 Hydrodynamics of fluid-solid coexistence in dense shear granular flow. *Phys. Rev.* E **75**, 051310.

KHAIN, E. & MEERSON, B. 2003 Onset of thermal convection in a horizontal layer of granular gas. *Phys. Rev.* E **67**, 021306.

KHAIN, E. & MEERSON, B. 2006 Shear-induced crystallization of a dense rapid granular flow: hydrodynamics beyond the melting point. *Phys. Rev.* E **73**, 061301.

KNOBLOCH, E. & PROCTOR, M. R. E. 1988 The double Hopf bifurcation with 2 : 1 resonance. *Proc. R. Soc. Lond.* A **415**, 61.

MANNEVILLE, P. 1990 *Dissipative Structures and Weak Turbulence.* Academic Press.

MIZUSHIMA, J. & GOTOH, K. 1985 Nonlinear stability of parallel flows. *J. Phys. Soc. Japan* **54**, 2061.

MOROZOV, A. N. & VAN SAARLOOS, W. 2007 An introductory essay on subcritical instabilities and the transition to turbulence in visco-elastic parallel shear flows. *Phys. Rep.* **447**, 112.

NEWELL, A. C. & WHITEHEAD, J. A. 1969 Finite bandwidth, finite amplitude convection. *J. Fluid Mech.* **38**, 279.

ORPE, A. V. & KHAKHAR, D. V. 2007 Rheology of surface granular flows. *J. Fluid Mech* **571**, 1.

PROCTOR, M. R. E. & JONES, C. A. 1988 The interaction of two spatially resonant patterns in thermal convection. Part 1. Exact 1 : 2 resonance. *J. Fluid Mech.* **188**, 301.

RAAFAT, T., HULIN, J. P. & HERRMANN, H. J. 1996 Density waves in dry granular media falling through a vertical pipe. *Phys. Rev.* E **53**, 4345.

REYNOLDS, W. C. & POTTER, M. C. 1967 Finite-amplitude instability of parallel shear flows. *J. Fluid Mech.* **27**, 465.

SAITOH, K. & HAYAKAWA, H. 2007 Rheology of a granular gas under a plane shear flow. *Phys. Rev.* E **75**, 021302.

SASVÁRI, M., KERTÉSZ, J. & WOLF, D. E. 2000 Instability of symmetric granular Couette flow in a granular gas: hydrodynamic field profiles and transport. *Phys. Rev.* E **62**, 3817.

SAVAGE, S. B. 1992 Instability of unbounded uniform granular shear flow. *J. Fluid Mech.* **241**, 109.

SCHIMD, P. J. & HENNINGSON, D. S. 2001 *Stability and Transition in Shear Flows.* Springer.

SELA, N. & GOLDHIRSCH, I. 1998 Hydrodynamic equations for rapid flows of smooth inelastic spheres, to Burnett order. *J. Fluid Mech.* **361**, 41.

SHUKLA, P. & ALAM, M. 2009 Landau-type order parameter equation for shear banding in granular Couette flow. *Phys. Rev. Lett.* **103**, 068001.

SHUKLA, P. & ALAM, M. 2011 Weakly nonlinear theory of shear-banding instability in granular Couette flow: analytical solution, comparison with numerics and bifurcation. *J. Fluid Mech.* **666**, 204.

STEWARTSON, K. & STUART, J. T. 1971 A non-linear instability theory for a wave system in plane Poiseuille flow. *J. Fluid Mech.* **48**, 529.

STUART, J. T. 1960 On the non-linear mechanics of wave disturbances in stable and unstable parallel flows. Part 1. The basic behaviour in plane Poiseuille flow. *J. Fluid Mech.* **9**, 353.

STUART, J. T. 1971 Nonlinear stability theory. *Annu. Rev. Fluid Mech.* **3**, 347.

SUSLOV, S. A. & PAOLUCCI, S. 1997 Nonlinear analysis of convection flow in a tall vertical enclosure under non-Boussinesq conditions. *J. Fluid Mech.* **344**, 1.

TAN, M.-L. 1995 Microstructures and macrostructures in rapid granular flows. PhD thesis, Princeton University, USA.

TAN, M.-L. & GOLDHIRSCH, I. 1997 Intercluster interactions in rapid granular shear flows. *Phys. Fluids* **9**, 856.

TSIMRING, L. S. & ARANSON, I. S. 1997 Localized and cellular patterns in a vibrated granular layer. *Phys. Rev. Lett.* **79**, 213.

UMBANHOWER, P., MELO, F. & SWINNEY, H. L. 1996 Localized excitations in a vertically vibrated granular layer. *Nature* **382**, 793.

WATSON, J. 1960 On the non-linear mechanics of wave disturbances in stable and unstable parallel flows. Part 2. The development of a solution for plane Poiseuille flow and for plane Couette flow. *J. Fluid Mech.* **9**, 371.